

Space Localisation Semester Project

Arion Zimmermann

Student Project at the Institute of Electrical and Micro Engineering
Spring 2022

Advisor : Andreas Burg
Co-advisor : Sitian Li
David Rodríguez

EPFL STI IEM TCL
ELD 131 (Bâtiment ELD)
Station 11

Contents

1	Introduction	1
2	Theoretical developments	2
2.1	Doppler effect	2
2.2	Channel modelisation	3
2.3	Feature extraction	5
2.4	Angle-of-Arrival estimator	7
2.5	Angle-of-Arrival estimation	9
3	Simulation results	15
3.1	Doppler effect validation	15
3.2	Exponential amplification	16
3.3	Error estimation	18
3.4	Finite Element Analysis	19
4	Experimental results	21
4.1	UWB radio prototype	22
4.1.1	System architecture	22
4.1.2	System design	25
4.1.3	Experimentation	28
4.2	USRP radio prototype	29
4.2.1	System architecture	29
4.2.2	System design	31
4.2.3	Experimentation	34
5	Future work	38
6	Conclusion	39
	List of terms	40

1 Introduction

Nowadays, many systems heavily depend on localisation technologies. Its rise was first driven by the defence industry. For a long time though, its full use was reserved to the US army and only a voluntarily degraded localisation was made available to the general public (with an accuracy of only 100m!). Nevertheless, with the rise of public awareness on this technology, the ability to obtain an absolute position estimate has proven to be an invaluable asset in many domains. In May 2000 [1], the US government allowed the general public to use the full capability of the GPS localisation system which could provide an accuracy down to 1m. From the automotive to the medical industries, this event marked a “boom” in research output about localisation systems, especially during the 00s.

A constellation of hundreds of GNSS satellites enables a global coverage on Earth. On other planets or in interplanetary space, however, localisation using Earth’s GNSS becomes much more difficult and is the subject of actual research [2]. Obtaining an absolute position on space vehicles is particularly critical since these vehicles are designed to operate semi-autonomously, as the time-delay to operate them from Earth is often too long.

Until now, positioning for these vehicles was mainly based on state-of-the-art sensor fusion [3]. The main drawback of this method is that small sensor bias might get integrated by the sensor fusion algorithm and introduce large errors over time. For a space vehicle, having an incorrect location estimate may lead to catastrophic consequences such as with USSR’s Luna 5 mission, as the semi-autonomous system would be more inclined to make erroneous decisions. Indeed, a bias on Luna 5’s gyroscope angular velocity made the guidance system believe that the spacecraft was spinning and performed the incorrect decision to compensate this spin [4]. This issue eventually led to the crash of Luna 5 on the surface of the Moon, which would have been avoided if an absolute angle reference had been available for the guidance system. In fact, absolute localisation would enable these type of algorithms to correct the state estimates and thereby enhance the safety and robustness of space vehicles.

The purpose of this project is to develop a technology deployable in areas without GNSS coverage that allows devices to locate themselves with respect to emitters anchored at well-known locations. A specific type of localisation was studied in this project: the angle-of-arrival (AoA). The idea is that multiple anchored emitters transmit a signal and that the space vehicle infers what is the angle between itself and the emitters. In particular, it was found that a rotating motion of the emitters generate a doppler effect that can be used to infer the AoA. This project pertained to study this phenomenon and to construct an highly accurate estimator for the AoA.

2 Theoretical developments

2.1 Doppler effect

Actual research on **AoA** localisation is focused on designing very specific antenna radiation patterns on the emitter side. The amplitude of the received signal is then proportional to this radiation pattern and can be used to infer the **AoA**. The major drawback of this method is that it mainly relies on the received signal amplitude, which is highly sensitive to noise and environmental effects. This project, however, encodes the **AoA**, not in the amplitude, but in the phase of the signal, so that it can avoid these types of errors.

It appears that it is possible to design an antenna with custom phase patterns but with much more difficulty than setting a gain pattern. This project proposes a new perspective for this problem: instead of trying to design an antenna with a custom phase pattern, a simple omnidirectional is put on a rotating motion, such that it generates a Doppler effect on the receiver side and emulates a custom antenna phase pattern.

Alice and Bob will be the main protagonist in the study of this system. Alice is considered as being the signal emitter and Bob receives that signal on his rotating antenna.

Now, let's recall the formalism of the doppler effect for an arbitrary signal emitted by Alice $a(t)$ and measured by Bob $b(t)$. Let $d(t)$ be the distance between the Alice and Bob.

After being emitted by Alice, the signal needs $\tau(t) = \frac{1}{c}d(t)$ time to reach Bob.

When Alice sends a signal, it can be decomposed into its eigenfrequencies f_i , such that $a(t) = \sum_{i=0}^{\infty} A_i(t) \exp(j2\pi f_i t)$, where $A_i(t)$ are arbitrary periodic complex functions that represent the amplitude and phase variations due to the antenna anisotropy.

When received by Bob, each of the frequency components $\exp(j2\pi f_i t)$ will be time-shifted by $\tau(t)$, such that equation (1) holds. This formulation will be exploited in the rest of the report.

$$b(t) = \sum_{i=0}^{\infty} A_i(t) \exp(j2\pi f_i(t - \tau)) \quad A_i(t) : \mathbb{R} \rightarrow \mathbb{C}, \quad f_i \in \mathbb{R} \quad (1)$$

Note that another formulation often seen in literature assumes that the signal sent by Alice has a single frequency component $a(t) = \exp(j2\pi f_c t)$ for which Bob receives $b(t) = \exp(j2\pi f_c(t - \tau))$. In this case, the signal phase reads $\tau(t) = t - \tau$ and the frequency drift can be derived as $f_{doppler}(t) = \frac{1}{2\pi} f(t) \frac{\partial}{\partial t} \phi(t) = f_c(1 - \frac{1}{c} \frac{\partial}{\partial t} d(t))$.

The idea of the project is to encode the localisation information into the signal delay $\tau(t)$ to estimate the location of Bob relative to Alice. There has been extensive research

in attempts to achieve localisation by having a constant τ depending on the distance between Alice and Bob, the method commonly known as **ToA** or **TDoA**. In parallel to that, some research has also been conducted for the **AoA** method. With this second method, τ is once again constant in time and depends on the absolute angle between Alice and Bob.

In this report, I propose a novel method to estimate the position of Bob. Instead of assuming that $\tau(t)$ is constant, I add a dependency on time by allowing Bob to move in space in a well-defined motion. Doing so will give Bob the ability to infer more information about his own location.

This project uses the effect of a circular motion on Bob's receiver that generates a Doppler shift. Further research may be performed for other kinds of motion.

2.2 Channel modelisation

Assume now that Bob is moving his antenna in a circular motion around himself at a frequency f_r .

We further assume that Alice, Bob and Bob's antenna lie in the same plane and call $\phi(t)$ the angle between them. The $\phi(t)$ angle will evolve in a circular motion: $\phi(t) = 2\pi f_r t + \phi_0$. Equation (2) shows the distance relation between Bob's antenna and Alice's antenna, where d_0 is the distance between Alice and Bob and r_0 is the distance between Bob and his antenna.

$$d^2(t) = d_0^2 + r_0^2 - 2d_0r_0 \cos(\phi(t)) \quad (2)$$

This $d(t)$ term expresses the distance between the two antennas. Changing the distance is equivalent to introducing a changing time delay:

$$\tau(t) = \frac{1}{c}d(t) = \frac{1}{c}\sqrt{d_0^2 + r_0^2 - 2d_0r_0 \cos(\phi(t))} \quad (3)$$

Now, combining equations (1) and (3), we see that Bob will receive Alice's signal according to the following equation:

$$b(t) = \sum_{i=0}^{\infty} A_i(t) \exp(j2\pi f_i(t - \frac{1}{c}\sqrt{d_0^2 + r_0^2 - 2d_0r_0 \cos(\phi(t))})) \quad (4)$$

Nevertheless, this equation does not take into the environmental effects on the channel. Indeed, random noise and multi-path effects can be included in this model.

Random noise can be simply modelled by an additive Gaussian white noise (**AWGN**) of power σ_w^2 .

In addition, clock synchronisation errors between Alice and Bob may occur. This error is generally modelled as an additional rotating phasor $\exp(j2\pi\Delta_f t)$.

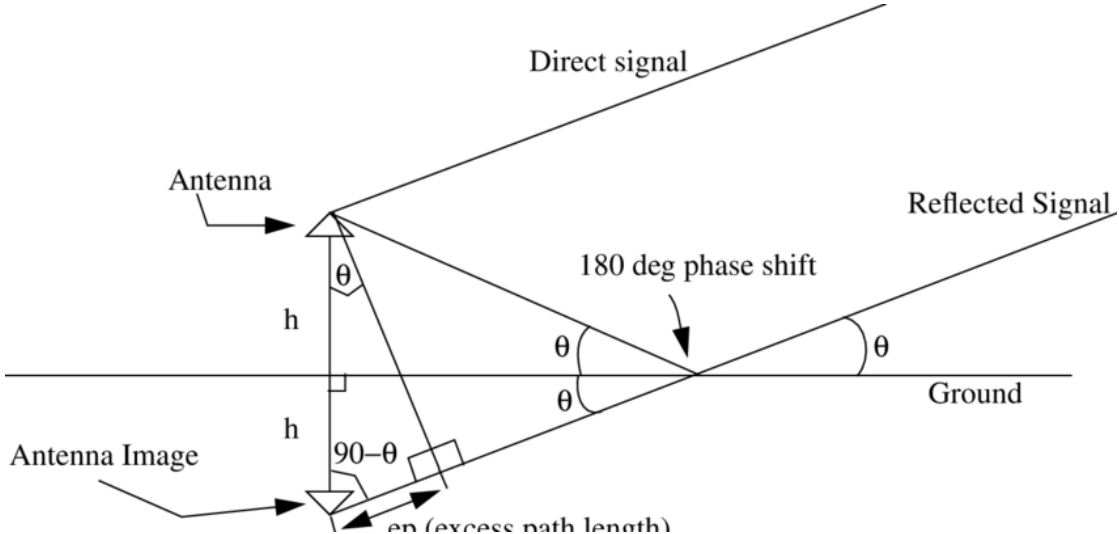


Figure 1: Multi-path geometry model

Since this project relates to localisation technologies for space applications, it can be assumed that the multi-path effects will be mainly resulting from ground reflections. From the drawing in figure 1, one may see that the additional time delay introduced depends on the distance between the Alice and the ground h_k . Multiple secondary paths indexed by k will be modelled. For every secondary signal path, the time delay now reads:

$$\tau_k(t) = \frac{1}{c}d_k(t) = \frac{1}{c}\sqrt{4h_k^2 + d_0^2 + r_0^2 - 2d_0r_0\cos(\phi(t))} \quad (5)$$

Of course, the amplitude of these secondary signals will be attenuated by the reflexion factor Γ_k , such that the reflected signal now reads:

$$b_k(t) = \sum_{i=0}^{\infty} \Gamma_k A_i(t) \exp(j2\pi f_i(t - \frac{1}{c}d_k(t))) \quad (6)$$

Putting all these undesirable effects together, the final signal perceived by Bob is now:

$$b(t) = \sum_k b_k(t) = \sum_k \sum_{i=0}^{\infty} \Gamma_k [A_i(t) \exp(j2\pi f_i(t - \frac{1}{c}d_k(t)) + j2\pi \Delta_f t) + \nu] \quad (7)$$

Equation (8) can be separated into three parts for every frequency component f_i . Each of these parts will be analysed separately in the next section.

Firstly, $\exp(j2\pi f_i t)$ is the passband signal that carries no information but helps Bob synchronise its local oscillator to Alice's oscillator thanks to a Phase-Locked Loop (**PLL**).

Secondly, the $\exp(-j2\pi f_i \frac{1}{c}(d_0))$ term carries the information about the distance between Alice and Bob. Extensive research was already done and is still being done [5] to optimally recover the d_0 from this term.

Finally, $\exp(j2\pi f_i \frac{1}{c}r_0 \cos(2\pi f_r t + \phi_0))$ contains the information of the relative angle between Alice and Bob. The method to analyse this term and recover the ϕ_0 is the main contribution of the research that was conducted this semester. Section 2.4 pertains at describing and analysing this method.

The separation between these three parts is considered as an engineering problem and will be treated in the following section.

2.3 Feature extraction

Given the signal modelled in equation (8), methods to recover the distance and the angle information by minimising the environmental effects will now be studied.

For the sake of simplicity, let's assume that Alice only sends a single frequency component f_c . This way, the received signal can be simplified to:

$$b(t) = \sum_k b_k(t) = \sum_k \Gamma_k [A_i(t) \exp(j2\pi f_c(t - \frac{1}{c}d_k(t)) + j2\pi \Delta_f t) + \nu] \quad (8)$$

Before separating the angle and distance information from the signal, there are multiple undesirable effects that must be dealt with: the Carrier Frequency Offset (**CFO**) Δ_f , the multi-path parameters Γ_k and d_k and the antenna variations $A_i(t)$. The random noise ν will be directly treated by the estimators.

To eliminate the **CFO** Δ_f , Bob is given a second antenna that must be placed at the center rotation of Bob's system. This way, two signals are received. The first one is affected by the Doppler effect as in equation (8). The second one only carries the delayed carrier frequency without any Doppler effect.

Now, if a **PLL** locks to the second signal, the carrier frequency phasor $b_2(t) = \exp(j2\pi f_{ct}t + j2\pi \Delta_f t)$ can be recovered.

Dividing the original signal $b(t)$ by $b_2(t)$ completely eliminates the **CFO** and converts the pass-band signal into base-band.

Methods to attenuate the multi-path have already been extensively researched and were not be further developed in this project. For instance, the use of autocorrelation of the incoming signal may be used to detect and reduce the secondary signal paths. [6] [7]

Without these environmental effects, the received signal now reads:

$$b(t) = A(t) \exp(-j2\pi f_c \frac{1}{c} d_k(t)) + \nu \quad (9)$$

The angle of the expression (27) can be extracted and squared, so that:

$$(\angle b(t))^2 = -(\angle A(t))^2 + 4\pi f_c^2 \frac{1}{c^2} (d_0^2 + r_0^2 - 2d_0 r_0 \cos(\phi(t))) + \nu' \quad (10)$$

Because of the operations involved in taking the complex angle and raising to a power, the distribution ν' is different from ν . The exact nature of ν' will be explained in the next section.

Now, the angle and distance information can be separated from each other. The average of $(\angle b(t))^2$ is $-\overline{\angle A^2} + 4\pi f_c^2 \frac{1}{c^2} (d_0^2 + r_0^2)$. With the apriori calibration of \bar{A} , it is possible to recover the distance d_0 between Alice and Bob.

Furthermore, the **AoA** can be isolated by removing the mean angle just obtained. For better readability, let $\delta^2 \angle A(t) = (\angle A(t))^2 - (\overline{\angle A})^2$. The resulting angle reads:

$$\theta(t) = (\angle b(t))^2 - \overline{(\angle b(t))^2} = \delta^2 \angle A(t) + 4\pi f_c^2 \frac{1}{c^2} (2d_0 r_0 \cos(\phi(t))) + \nu' \quad (11)$$

A first glance at equation (29) may suggest that the **AoA** can be easily retrieved using a least-squares method such as in [8]. Nevertheless, the phase variations $\delta \angle A(t)$ may alter the result that would be provided by such an estimator.

This motivated the need to design a novel estimator that could completely ignore the $\delta^2 \angle A(t)$ error. This estimator uses the two key properties of $\delta^2 \angle A(t)$:

Periodicity $\delta^2 \angle A(t)$ is a periodic signal with the same period as the antenna rotation.

Parity When the angle between Alice, Bob and Bob's antenna is zero ($\phi = 0$), then it does not matter if the antenna starts rotating clockwise or counter-clockwise. Algebraically, this property is the even parity of the phase variations: $\delta^2 \angle A(t) = \delta^2 \angle A(-t)$.

Although these properties may be extremely generic, they are key to building an estimator that counters these phase variations.

A step that may seem arbitrary at first consists of performing the following operation. The reason for this operation will soon become obvious.

$$s(t) = \exp(\theta(t) + j\theta(t - \frac{1}{4f_r})) \quad (12)$$

Since $\delta^2 \angle A(t)$ is a periodic function and has even parity by definition, it can be written in terms of its Fourier series:

$$\delta^2 \angle A(t) = \sum_{n=1}^{\infty} C_n \cos(2\pi f_r n t + \phi) , \quad C_n \in \mathbb{R} \quad (13)$$

Applying the operation in (30) for the phase variations yields:

$$\delta \angle A(t) = \exp(j\phi) \sum_{n=1}^{\infty} C_n \exp(j2\pi f_r n t) \quad (14)$$

Finally, the processed signal reads:

$$s(t) = \exp(\exp(j\phi)) \sum_{n=1}^{\infty} C_n \exp(j2\pi f_r n t) + 4\pi f_c^2 \frac{1}{c^2} (2d_0 r_0 \exp(j\phi(t))) + \nu'' \quad (15)$$

We will see in the next section that putting the signal in the form (2.5) enables the discovery of an optimal estimator for the **AoA**. In this project, the operation performed with (30) is called the "Exponential Amplification".

2.4 Angle-of-Arrival estimator

Before constructing the estimators for the **AoA** as perceived by Bob, it is necessary to develop a few mathematical tools that will help studying the variance of these estimators.

A general statement that simplifies the analysis of these estimators can first be established. Indeed, the idea is that all the information of a periodic signal is contained in single periods of this signal and that it is sufficient to find an estimator for a single period to construct an optimal general estimator. The following theorem formalises this idea.

Theorem 1. Let $X_t \sim f_X(x, t)$ represent measurements from a periodic signal. Define $\hat{\phi}$ as an estimator for a parameter of $\mu(t)$ and $\hat{\phi}_p$ as the estimator. If $\hat{\phi}_p$ can reach the Cramer-Rao bound for single periods with the estimator $\hat{\phi}_0$, then there exists an optimal estimator $\text{Var}(\hat{\phi}) = \frac{1}{N} \text{Var}(\hat{\phi}_0)$.

Proof. Let \vec{Z} denote the random vector that represents the concatenation between all the measurements between t_0 and $t_0 + T$, where t_0 is an arbitrary starting time and T is the period of the signal.

Let $E = \{\vec{e}_i\}$ be an index set that spans the time in a signal period. The dimension of \vec{Z} must match the dimension of E . In addition, define the bijective time-mapping function $t : E \rightarrow \mathbb{R}$. With this formalism, the distribution of Z can then be written as in equation (16)

$$\vec{Z}|t_0 \sim f_Z(\vec{x}|t_0) = \sum_{e_i \in E} f_X(\vec{x}^T \vec{e}_i, t_0 + t(\vec{e}_i)) \vec{e}_i \quad (16)$$

In particular, we can define two random vectors $Z_1 \sim f_Z(\vec{x}|t_0)$ and $Z_2 \sim f_Z(\vec{x}|t_0+T)$. However, by the periodicity of the distribution f_X over a period T , we get that Z_1 and Z_2 actually follow the same distribution $f_Z(\vec{x}|t_0)$. Z_1 and Z_2 then satisfy the definition of identically distributed random vectors. In addition, the vectors $Z_i|t_0$ are independent from each other.

To conclude the proof, observe that the fisher information contained in N periods is N times the fisher information of a single period: $I(\hat{\phi}) = NI(\hat{\phi}_i)$. Since ϕ_i satisfies the Cramer-Rao bound, we have that:

$$Var(\hat{\phi}) \geq \frac{1}{N} I(\hat{\phi}_i) = \frac{1}{N} Var(\hat{\phi}_i) \quad (17)$$

The existence of such an estimator is implied by the construction $\hat{\phi} = \frac{1}{N} \sum_{i=1}^N \hat{\phi}_i$ and its variance is $Var(\hat{\phi}) = \frac{1}{N} Var(\hat{\phi}_i)$ by the central limit theorem. This estimator reaches the lower bound found in equation (17) and thus proves the theorem. \square

Before starting to analyse the estimators for the relative angle and distance, a channel model must be derived. We assume that a signal of interest is affected by an **AWGN** following a distribution $\nu \sim N_{\mathbb{C}}(0, \sigma_w^2)$. The expression (18) represents the distribution for a single sample.

$$X(t) \sim f_X(x|t) = \frac{1}{\sigma_w \sqrt{2\pi}} \exp\left(-\frac{1}{2\sigma_w^2}(y - b(t))^2\right) \quad (18)$$

We now want to generalise this distribution, so that every signal period is considered as a single random variable Z . Let the period $T = \frac{1}{f_r}$

In the same manner as the preceding theorem, a basis index set $E = \{\vec{e}_i\}$ and a bijective time-mapping function $t : E \rightarrow [0, T]$ can be defined. Let $\vec{\mu} = \sum_{\vec{e}_i \in E} b(t(\vec{e}_i)) \vec{e}_i = \sum_{\vec{e}_i \in E} \mu_i \vec{e}_i$, where the notation was simplified by setting $\mu_i = b(t(\vec{e}_i))$. Then, the distribution of Z can be formalised as in equation (19):

$$\vec{Z} \sim f_Z(\vec{x}) = N(\vec{\mu}, \sigma_w) \quad (19)$$

A last important result pertaining to estimate the optimal variance of the distance and phase estimators must be derived.

Theorem 2. *Let $Z \sim N(\vec{\mu}, \sigma_w^2)$. For any parameter ϕ that affects $\vec{\mu}$, the variance of the estimator for that parameter is lower-bounded by $(\sum_{\vec{e}_i \in E} \frac{1}{\sigma_w^2} (\frac{\partial}{\partial \phi} \mu_i)^2)^{-1}$*

Proof. The Fisher information contained in $Z \sim f_Z(z; \phi)$ is defined as:

$$I(\phi) = E\left[\frac{\partial^2}{\partial \phi^2} \ln(f_Z(z; \phi))\right] \quad (20)$$

. Since $Z \sim N(\vec{\mu}, \sigma_w^2)$, the Fisher information can be evaluated to:

$$I(\phi) = (\frac{\partial \vec{\mu}}{\partial \phi})^T \frac{1}{\sigma_w^2} (\frac{\partial \vec{\mu}}{\partial \phi}) = \sum_{\vec{e}_i \in E} \frac{1}{\sigma_w^2} (\frac{\partial}{\partial \phi} \mu_i)^2 \quad (21)$$

Now, since samples drawn from Z are independent and identically distributed, the Cramer-Rao bound holds and the following statement is true:

$$Var(\hat{\phi}) \geq \frac{1}{I(\phi)} \quad (22)$$

Putting equations (21) and (22) together proves the statement. \square

2.5 Angle-of-Arrival estimation

After this interlude of small mathematical tools, the **AoA** can be estimated. Recall the expression from (2.5):

$$s(t) = \exp(j\phi) \exp\left(\sum_{n=1}^{\infty} C_n \exp(j2\pi f_r n t) + 4\pi f_c^2 \frac{1}{c^2} (2d_0 r_0 \exp(j\phi(t)))\right) + \nu''$$

For the sake of conciseness, we can rewrite this expression by defining the $\alpha = 4\pi f_c^2 \frac{r_0 d_0}{c^2}$ and the angular speed $\omega = 2\pi f_r t$, such that the following expressions are obtained:

$$\phi(t) = \omega t + \phi s(t) = \exp(j\phi) \exp\left(\sum_{n=1}^{\infty} C_n \exp(j\omega n t) + \alpha \exp(j\phi) \exp(j\omega t)\right) + \nu'' \quad (23)$$

We have shown in section 2.3 that the received signal can be put in the form of equation .

Here, ν'' is the **AWGN** distribution for the processed signal $s(t)$. The following paragraph will be dedicated to establishing its nature. But beforehand, the following lemma might be useful to prove:

Lemma 1. *The signal model $s = A \exp(ix) + \nu$ is equivalent to $A(1 + Re[\nu]) \exp(ix + i\frac{Im[\nu]}{A})$ for $A \in \mathbb{R}$, $x \in \mathbb{R}$, $\nu \sim N_{\mathbb{C}}(0, \sigma_w^2)$ and $\frac{A}{\nu} \rightarrow 0$.*

Proof. Consider the Euclidian representation of complex numbers. To simplify the notation, we write vectors \vec{v} with a subscript \vec{v}_c , when the vector is represented in cartesian

coordinates and with a subscript \vec{v}_p for polar coordinates.

Let \vec{A} represent the information signal. In polar coordinates, $\vec{A}_p = [A \ x]^T$. Let $\vec{\nu}$ represent a random vector for which the coordinates read $\vec{\nu}_c = [Re[\nu] \ Im[\nu]]^T$. Finally, let $\vec{s}_p = \vec{A}_p + \vec{\nu}_c$ be the resulting vector.

The idea now is to express $\vec{\nu}_c$ as a polar vector $\vec{\nu}_p = [\delta r \ \delta\theta]^T = \vec{e}_r^T \vec{\nu}_c \vec{e}_r + \frac{1}{r} \vec{e}_\theta^T \vec{\nu}_c \vec{e}_\theta$, where \vec{e}_θ and \vec{e}_r are the basis vectors in polar coordinates. Note that the $\frac{1}{r}$ term was necessary to normalize the angular unit vector, so that it always has the same length, regardless of the value of r .

The distribution of the projections $\delta r = \frac{\partial r}{\partial x} \vec{e}_r^T \vec{\nu}_c$ and $\delta\theta = \vec{e}_\theta^T \vec{\nu}_c$ must be computed. The following relation between unit vectors holds:

$$\begin{bmatrix} \vec{e}_r \\ \vec{e}_\theta \end{bmatrix} = \begin{bmatrix} \cos(\theta) & \sin(\theta) \\ -\sin(\theta) & \cos(\theta) \end{bmatrix} \begin{bmatrix} \vec{e}_x \\ \vec{e}_y \end{bmatrix} \quad (24)$$

This transformation is simply a rotation of the unit vectors. Luckily, we can show that the distribution $\nu \sim N^C(0, \sigma_w^2)$ is invariant under rotations.

Indeed, the joint distribution $\nu \sim f(x, y)$ can be written reads:

$$f(x, y) = \frac{1}{\sigma_w^2 \pi} \exp\left(-\frac{1}{\sigma_w^2} x^2\right) \exp\left(-\frac{1}{\sigma_w^2} y^2\right) = \frac{1}{\sigma_w^2 \pi} \exp\left(-\frac{1}{\sigma_w^2} (x^2 + y^2)\right) \quad (25)$$

Equation (25) highlights that the probability density f depends exclusively on $x^2 + y^2 = r^2$. Rotating the coordinates will therefore not change the distribution.

Coming back to equation (24), we get:

$$\vec{\nu}_p = [\delta r \ \delta\theta]^T = \vec{e}_r^T \vec{\nu}_c \vec{e}_r + \frac{1}{r} \vec{e}_\theta^T \vec{\nu}_c \vec{e}_\theta = [Re[\nu] \ \frac{1}{r} Im[\nu]]^T \quad (26)$$

Finally, $\vec{s}_p = \vec{A}_p + \vec{\nu}_p = [A + Re[\nu] \ x + \frac{1}{r} Im[\nu]]^T$, which proves the lemma since $s = A(1 + Re[\nu]) \exp(ix + i\frac{Im[\nu]}{A})$

□

The objective is now to find the distribution of ν'' in equation (2.5). Recall that the original noise ν was transformed into ν' because of the following steps:

$$b(t) = A(t) \exp(-j2\pi f_c \frac{1}{c} d_k(t)) + \nu \quad (27)$$

$$(\angle b(t))^2 = -(\angle A(t))^2 + 4\pi f_c^2 \frac{1}{c^2} (d_0^2 + r_0^2 - 2d_0 r_0 \cos(\phi(t))) + \nu' \quad (28)$$

$$\theta(t) = (\angle b(t))^2 - (\angle b(t))^2 = \delta \angle A(t) + 4\pi f_c^2 \frac{1}{c^2} (2d_0 r_0 \cos(\phi(t))) + \nu' \quad (29)$$

$$s(t) = \exp(\theta(t) + j\theta(t - \frac{1}{4f_r})) \quad (30)$$

Applying lemma (1) for equation (27), we find that the noise on the squared angle $\angle b(t)^2$ can be upper-bounded by:

$$\nu' \leq 8\pi \frac{f_c^2}{c^2} (d_0 + r_0)\nu + \nu^2$$

This expression for ν' is difficult to handle, since it depends on both ν and ν^2 . Thus, assuming that $\frac{f_c^2}{c^2} d_0 \gg \frac{f_c^2}{c^2} r_0 \gg 1$, it can be simplified to:

$$\nu' \approx 8\pi \frac{f_c^2}{c^2} (d_0)\nu = \alpha\nu$$

Equation (30) exponentially amplifies the noise ν' to ν'' . We will see in the next paragraph that only the magnitude of this noise affects the **AoA** estimator. In this case, since the noise amplitude is with high probability much lower than $\exp(\theta(t))$, the following first-order approximation holds:

$$|s(t)| \approx |\exp(\theta(t) + \nu')| \approx \exp(\theta(t))(1 + \nu')$$

The amplitude of $s(t)$ is therefore roughly affected by an **AWGN** of magnitude $2\exp(\theta(t))\alpha\sigma_w$. All along these calculations, the difficulty to analyse operations on random variables imposed the use of approximations. Nevertheless, the validity of these approximations were individually assessed on Matlab.

Let's come back to the original problem. Given a signal $s(t)$ from equation (23):

$$s(t) = \exp(\exp(j\phi) \sum_{n=1}^{\infty} C_n \exp(j\omega nt) + \alpha \exp(j\omega t)) + \nu''$$

, there are now two main questions that must be answered.

Firstly, what is the variance of an optimal estimator for the **AoA** ϕ ?

Secondly, how can we construct an estimator that indeed achieves this lower bound?

To answer the first question, the theorem (2) can be used with the basis index set $E = \{e_i : i \in \mathbb{R}\}$ and the uniform time-mapping function $t(e_i) = \frac{i}{T}$ to find the variance of an optimal estimator $\hat{\phi}_{opt}$, if it exists. It is also assumed that an optimal estimator can eliminate the phase variations $\sum_{n=1}^{\infty} C_n \exp(j\omega nt)$.

$$\begin{aligned}
Var(\hat{\phi}_{opt}) &= \frac{1}{I(\phi)} = \left[\sum_{\vec{e}_i \in E} \frac{1}{Var[\nu'']} \left(\frac{\partial}{\partial \phi} \mu_i \right)^2 \right]^{-1} = \left[\frac{1}{T} \int_0^T \frac{1}{Var[\nu'']} \left| \frac{\partial}{\partial \phi} s^*(t) \right|^2 dt \right]^{-1} \\
&= \left[\frac{1}{T} \int_0^T \frac{1}{2\alpha \exp(2\alpha \cos(j\omega t + j\phi))} \left| \exp(2\alpha \exp(j\omega t + j\phi)) \exp(2j\omega t + 2j\phi) \right| dt \right]^{-1} \\
&= \sigma_w^2 \left[\alpha \frac{1}{T} \int_0^T \exp(2i\alpha \sin(\omega t + \phi)) dt \right]^{-1} = \frac{\sigma_w^2}{\alpha}
\end{aligned} \tag{31}$$

The variance of estimator is proportionally decreasing, as α gets larger. This fact is extremely interesting because it means that a physical design parameter can arbitrarily increase the accuracy of an optimal estimator.

The only part that remains is to prove the existence of such an estimator and construct it.

To achieve this goal, a new mathematical framework was developed making use of a so-called Digamma transform.

Definition 1. Let F_g be the following transformation of an arbitrary function g :

$$F_g(n) = \frac{\omega}{2\pi} \int_0^{2\pi/\omega} g(\alpha \exp(j\omega t + j\phi)) e^{-j\omega nt} dt \tag{32}$$

A few properties of this transform will be proven in the following paragraph.

Lemma 2. The digamma transform obeys the orthogonality relation: $\langle F_g(n) | F_g(n') \rangle = K_{nn'} \delta_{nn'}$. for every $n, n' \in \mathbb{N}$, $K_{nn'} \in \mathbb{C}$ and the basis function $g(z) = z^m$, $m \in \mathbb{N}$.

Proof.

$$\langle F_g(n) | F_g(n') \rangle = \frac{\omega^2}{(2\pi)^2} \int_0^{2\pi/\omega} \int_0^{2\pi/\omega} (\exp(j\phi) \exp(-j\phi))^m e^{j\omega((n+m)t - (n'+m)t')} dt dt'$$

□

Lemma 3. For any holomorphic function $g : \mathbb{C} \rightarrow \mathbb{C}$, $F_g(n) = \frac{\alpha^n \exp(jn\phi)}{n!} \lim_{\tau \rightarrow 0} \frac{d^n}{d\tau^n} g(\tau)$.

Proof. With a change of variable $\tau = \exp(i\omega t)$, $dt = \frac{1}{i\omega\tau} d\tau$, $\gamma = \{z \in \mathbb{C} : z = \exp(it), t \in [0, 2\pi]\}$ and using Cauchy's residue theorem, we obtain:

$$F_g(n) = \frac{1}{2\pi} \int_{\gamma} g(\alpha\tau) \frac{1}{i\tau^{n+1}} d\tau = \frac{1}{n!} \lim_{\tau \rightarrow 0} \frac{d^n}{d\tau^n} g(\alpha\tau) = \frac{\alpha^n}{n!} \lim_{\tau \rightarrow 0} \frac{d^n}{d\tau^n} g(\tau)$$

□

This Digamma transform can now be used to analyse the signal of interest

$$s(t) = \exp\left(\sum_{n=1}^{\infty} C_n \exp(j\omega nt) + \alpha \exp(j\omega t)\right) + \nu''$$

With a change of variable $\tau = \exp(j\omega t)$, the signal to transform reads:

$$g(\tau) = \exp(\alpha \exp(j\phi) [\frac{1}{\alpha} \sum_{n=1}^{\infty} C_n \tau^n + \tau]) + \nu'$$

Finally, the Digamma transform can be applied:

$$\mathcal{F}_g(n) = \frac{\omega}{2\pi} \int_0^{2\pi/\omega} g(t) e^{-j\omega nt} dt = A_0 \frac{\exp(jn\phi)(\alpha)^n}{n!} \lim_{\tau \rightarrow 0} \frac{d^n}{d\tau^n} \exp[\frac{1}{\alpha} \sum_{n=1}^{\infty} C_n \tau^n + \tau] + \frac{\omega}{2\pi} \nu'$$

Since the term $\lim_{\tau \rightarrow 0} \frac{d^n}{d\tau^n} \exp[\frac{1}{\alpha} \sum_{n=1}^{\infty} C_n \tau^n + \tau]$ does not depend on the **AoA**, a calibration process can estimate it and compensate it. This way, the Digamma estimator has successfully removed the antenna phase variations.

Finally, the **AoA** can be estimated using:

$$\hat{\phi}_n = \frac{\angle \mathcal{F}_{\exp}(n)}{n} - \pi/2 + \nu'''$$

The distribution of ν''' can be found using the lemma (1) when assuming that ν'' is a Gaussian random variable with variance $2 \exp(\theta(t)) \alpha \sigma_w$ and applying the digamma transform on it. In this case,

$$\text{Var}[\nu'''] = \frac{\omega}{2\pi} \frac{n!}{\alpha^n} \sigma_w^2 \int_0^{2\pi/\omega} e^\theta(t) e^{-j\omega nt} dt = \frac{n!}{\alpha^n} I_n(2\alpha) * \sigma_w^2$$

Here, $I_n(2\alpha)$ is the modified Bessel function:

$$I_\alpha(x) = \sum_{m=0}^{\infty} \frac{1}{m! \Gamma(m+\alpha+1)} \left(\frac{x}{2}\right)^{2m+\alpha} \quad (33)$$

It can be shown that the Bessel function $I_n(x) \leq I_0(x)$ for every x . Hence,

$$\text{Var}[\nu'''] \leq \frac{n!}{\alpha^n} I_0(2\alpha) * \sigma_w^2 \quad (34)$$

Since we have shown in lemma (2.5) that the digamma transform obeys an orthogonality relation for different n , we can consider $\hat{\phi}_n$ as independent random variables with respect to n . The different ϕ_n estimates can be merged together through a convex combination $\hat{\phi}_\tau = \sum_{n=0}^{\infty} \gamma_n \hat{\phi}_n$ with $\sum_{n=0}^{\infty} \gamma_n = 1$.

Lemma 4. *Assume $\hat{\phi}_n \sim N(0, \sigma_n^2)$. There exists a vector γ such that $\hat{\phi}_\tau = \sum_{n=0}^{\infty} \gamma_n \hat{\phi}_n$ has a standard deviation of $(\sum_{n=0}^{\infty} \frac{1}{\sigma_n^2})^{-1/2}$*

Proof. The linear form of ϕ_τ allows to define the following linear optimisation problem:

$$\min_{\gamma} \text{Var}(\hat{\phi}_\tau) = \min_{\gamma} \sum_{n=0}^{\infty} \gamma_n^2 \sigma_n^2, \quad \sum_{n=0}^{\infty} \gamma_n = 1$$

Since this is a linear convex problem, the KKT conditions will be necessary and sufficient to find an optimal $\tilde{\gamma}$ vector: $2\tilde{\gamma}_n\sigma_n^2 - 2\lambda = 0$, $\lambda \in \mathbb{R}$ $\forall n \in \mathbb{N}$.

This implies that $\tilde{\gamma}_n = \frac{\lambda}{\sigma_n^2}$ and $\frac{1}{\lambda} = \sum_{n=0}^{\infty} \frac{1}{\sigma_n^2}$. Combing the above equations, we obtain the following expression for the minimum variance:

$$\min_{\gamma} \text{Var}(\hat{\phi}_{\tau}) = \lambda^2 \sum_{n=0}^{\infty} \frac{1}{\sigma_n^2} = \left(\sum_{n=0}^{\infty} \frac{1}{\sigma_n^2} \right)^{-1}$$

Taking the square root from both sides finishes the proof. \square

Applying this lemma to the original problem, the term $\sum_{n=0}^{\infty} \frac{1}{\sigma_n^2}$ becomes:

$$\sum_{n=0}^{\infty} \frac{1}{\sigma_n^2} = \frac{1}{\alpha \sigma_w^2 \exp(2\alpha)} \sum_{n=0}^{\infty} \left(\frac{\alpha^n}{n!} \right)^2$$

Here, the following theorem can be used:

Theorem 3. Parseval-Gutzmer Let f be an analytic function on a closed disk of radius r with Taylor series $f(z) = \sum_{k=0}^{\infty} a_k z^k$. Then,

$$\frac{1}{2\pi} \int_0^{2\pi} |f(re^{i\theta})|^2 d\theta = \sum_{k=0}^{\infty} |a_k r^k|^2$$

Applying this theorem for $r = \alpha$ and $a_k = \frac{1}{n!}$, the following equality holds:

$$\begin{aligned} \sum_{n=0}^{\infty} \frac{1}{\sigma_n^2} &= \frac{\alpha}{\sigma_w^2 \exp(2\alpha)} \frac{1}{2\pi} \int_0^{2\pi} |\exp(re^{j\theta})|^2 d\theta \\ &= \frac{\alpha}{\sigma_w^2 I_0(2\alpha)} \frac{1}{2\pi} \int_0^{2\pi} \exp(2r \cos(\theta)) d\theta \\ &= \frac{\alpha}{\sigma_w^2 I_0(2\alpha)} I_0(2\alpha) = \frac{\alpha}{\sigma_w^2} \end{aligned}$$

where $I_{\alpha}(x)$ is the modified Bessel function, as in (33).

Recalling that the Cramer-Rao lower bound for this estimator was $\frac{\alpha}{\sigma_w^2}$ in equation (31) and observing that Digamma estimator estimator variance is upper bounded by $\frac{\alpha}{\sigma_w^2}$.

To sum up, the Digamma estimator is an optimal estimator for the AoA between Alice and Bob. It asymptotically achieves the Cramer-Rao bound and, in addition, eliminates undesired phase variations on the received signal. This standard error on the AoA finally reads:

$$\sigma_{opt} = \frac{\sigma_w}{\sqrt{\alpha}} = \frac{\sigma_w}{2\pi f_c \frac{\sqrt{r_0 d_0}}{c}}$$

3 Simulation results

Multiple Matlab simulations were performed to validate the theory developed for this project. The most relevant ones will be described in this section. Firstly, the effect of a rotating signal source was studied. The resulting signal was compared to the theory. Then, the effect of the “exponential amplification” operation was studied. Finally, the environmental effects were added to the model and simulated.

3.1 Doppler effect validation

The first simulation pertained to show the relation between **AoA** and signal shape. Multiple simulations were performed for different angles-of-arrival and carrier frequencies. The distance between emitter and receiver was maintained at 1m and the rotation radius of the rotating antenna was set at 10cm.

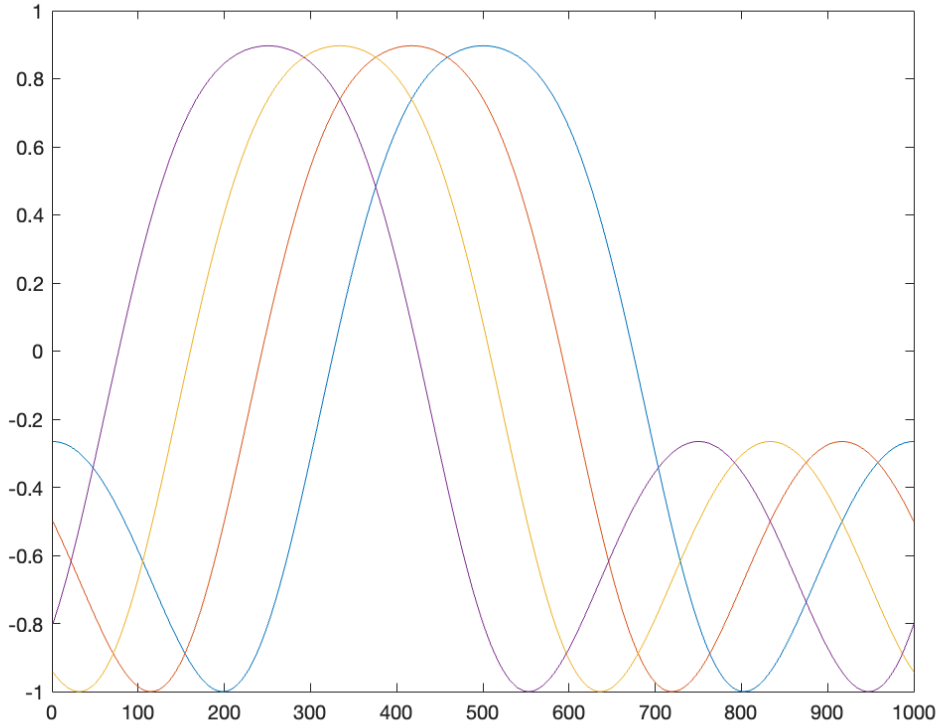


Figure 2: Received signal for multiple **AoAs** at 1200MHz carrier frequency

On the one hand, the first figure depicts the resulting signals affected by the doppler effect for a carrier frequency of 1200MHz. The signal shape indeed complies with the

theory and four different angles-of-arrival (0° , 30° , 60° , 90°) could be differentiated.

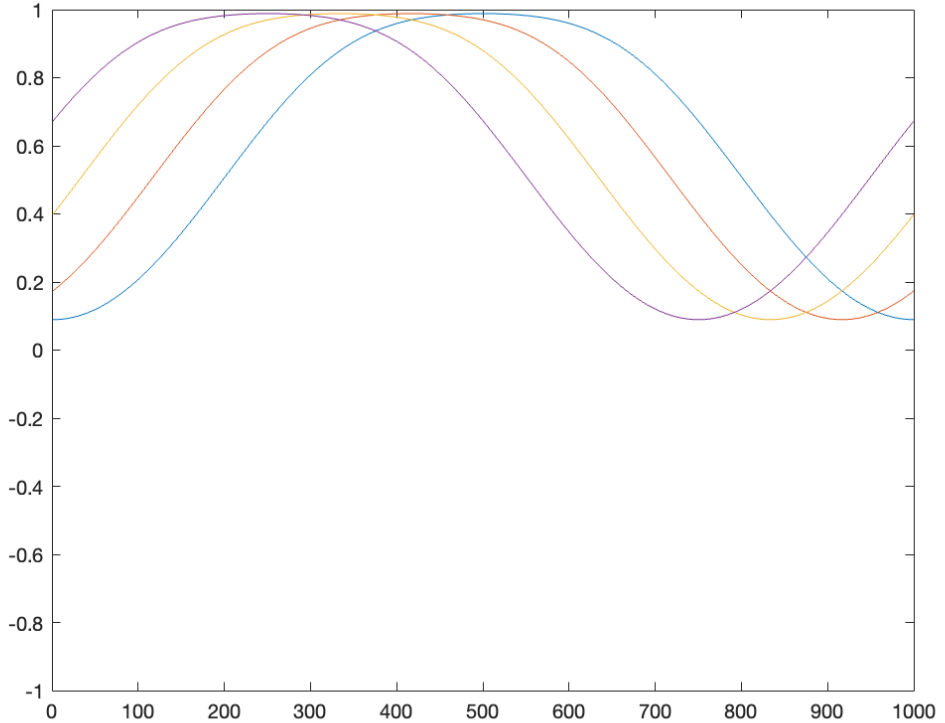


Figure 3: Received signal for multiple AoAs at 400MHz carrier frequency

The second figure plots the same signal, yet the carrier frequency was reduced to 400MHz. Remark that the signal variance was reduced, thereby implying that the Fisher information contained in this second signal has decayed. This phenomenon was also expected by the theory, since the fisher information is proportional to the carrier frequency.

3.2 Exponential amplification

The purpose of the exponential amplification is to amplify the signal where it is already high, so that it can be further used with the digamma transform to estimate the AoA. Using the same condition as in figure 2, the result of the exponential amplification operation could be plotted for the four different angles-of-arrival (0° , 30° , 60° , 90°) and a carrier frequency of 1200MHz.

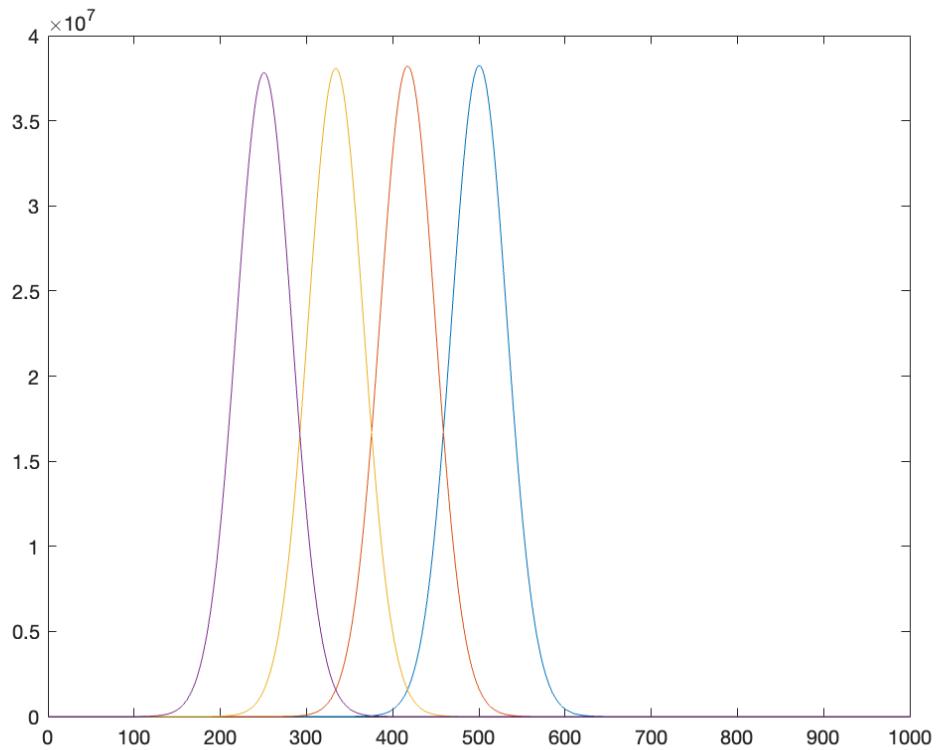


Figure 4: Exponential amplification for 1200MHz carrier

The four signals in figure 4 are now more easily differentiated than in figure 2. Note that even though it seems that the accuracy in AoA estimation has increased, the fisher information has not. In other words, if random noise is added to the signal before the exponential amplification, the noise will also be amplified. Figure 5 illustrates well this behaviour for a noise power of 10dBm. To sum up, the exponential amplification does not add information to the signal, but only transforms it, so that it can be more easily processed by the next steps.

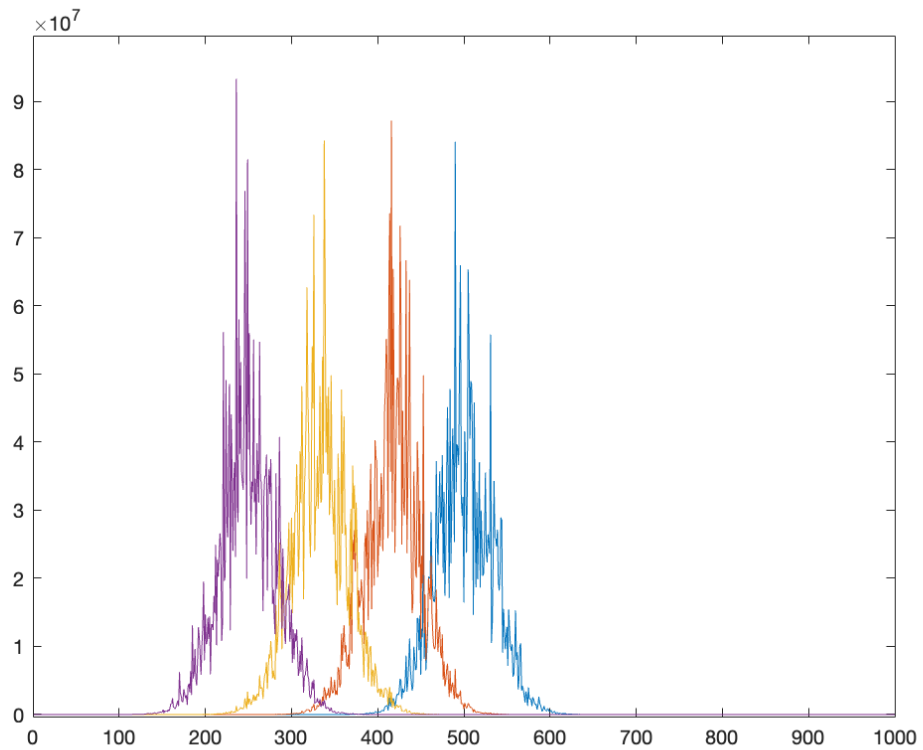


Figure 5: Exponential amplification for 1200MHz carrier with 10dB noise

3.3 Error estimation

The whole **AoA** estimator was simulated in the presence of **AWGN**. The resulting estimator variance was plotted with respect to the SNR at the reception of the signal.

The relation between SNR and estimator variance effectively complies with the theory as it shows a inversely proportional behaviour against the design parameters r_0 , f_c and d_0 . Figure 6 compares the theoretical behaviour and the simulated behaviour.

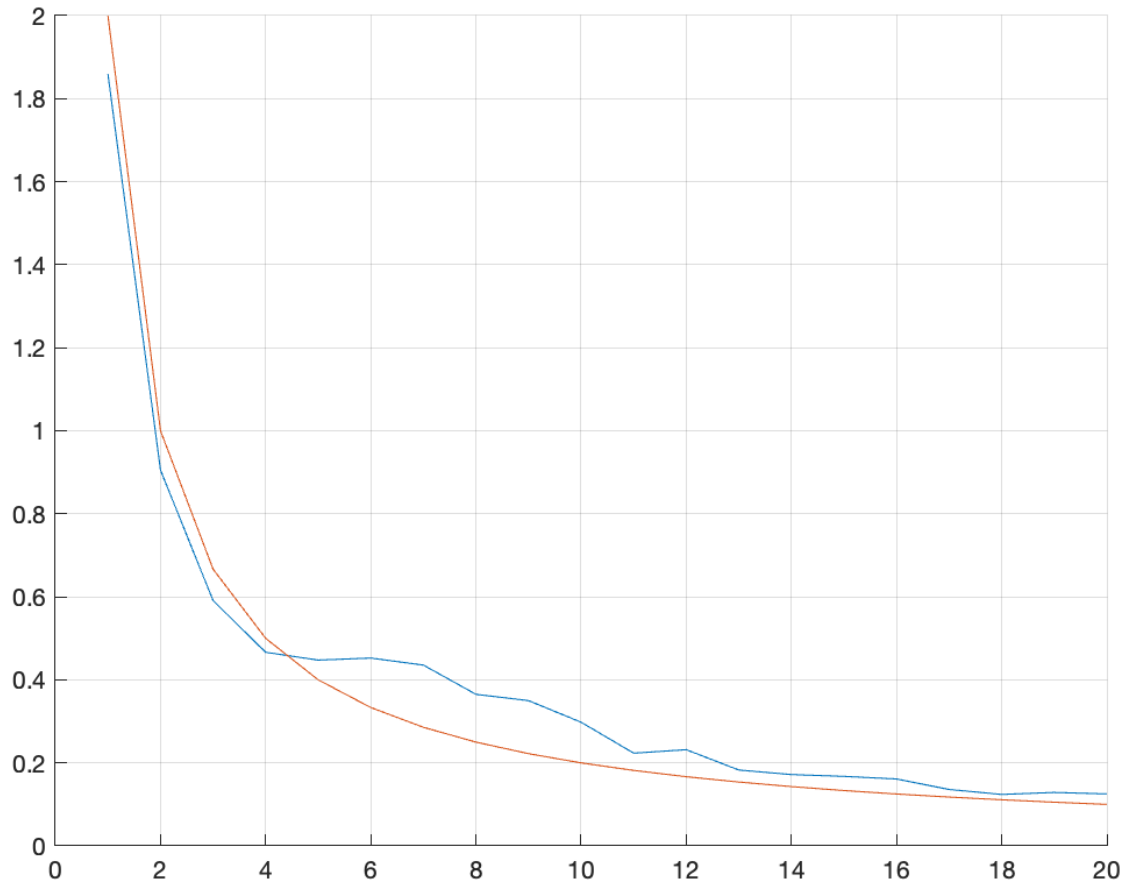


Figure 6: Estimator variance comparison (red: theoretical $\frac{1}{\alpha}$ behaviour); blue: simulated behaviour with the Digamma estimator

3.4 Finite Element Analysis

The last simulation that was performed attempted to assess the performance of the AoA estimator in the presence of multi-path effects. For this, a physical simulator, which solves the 2D wave equation, was developed. Arbitrary obstacles and their reflection factor could be added to the simulator. A visualisation of the resulting wave is depicted in figure 7.

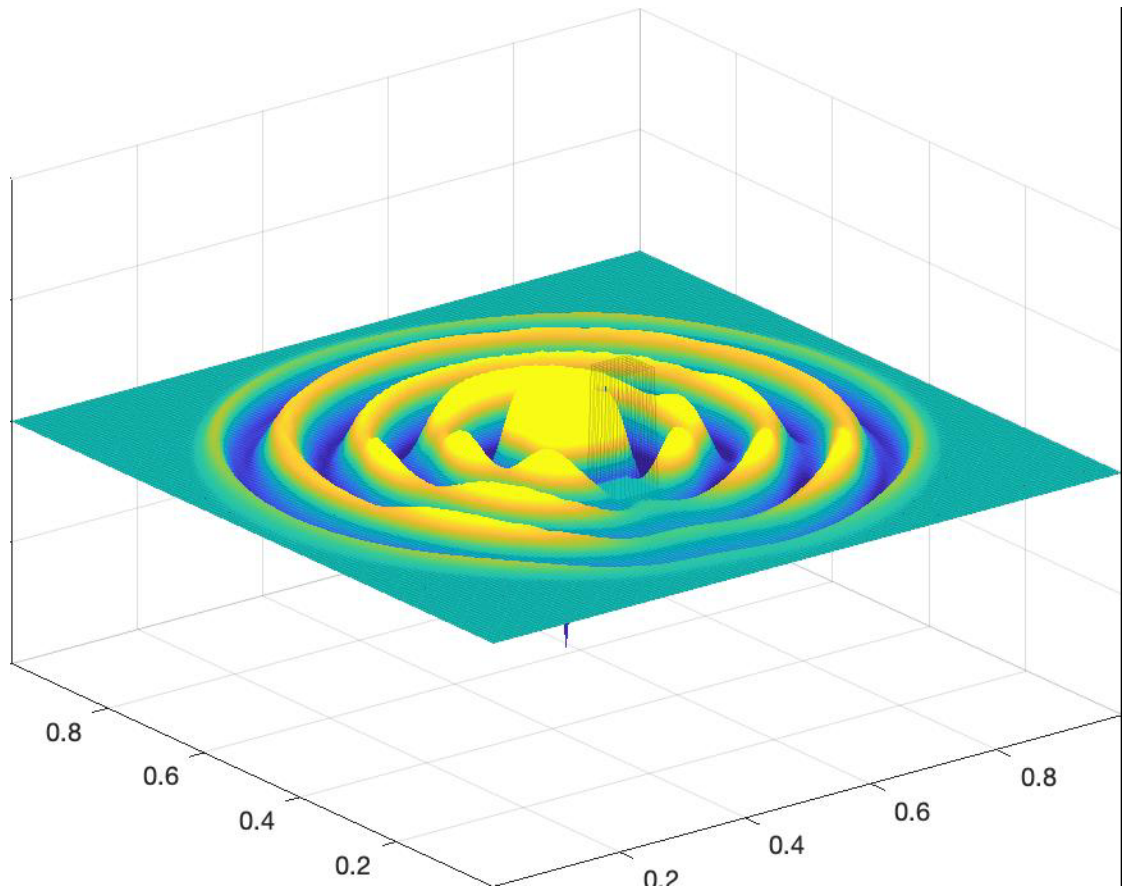


Figure 7: Multi-path simulation with single obstacle

For this project, no mitigation strategy to prevent multi-path was implemented, since it is a subject which has already been widely studied [6] [7]. Nonetheless, this simulation could give a better insight in the error that could be expected because of multi-path. In fact, the error introduced by the simulated multi-path effect could be plotted.

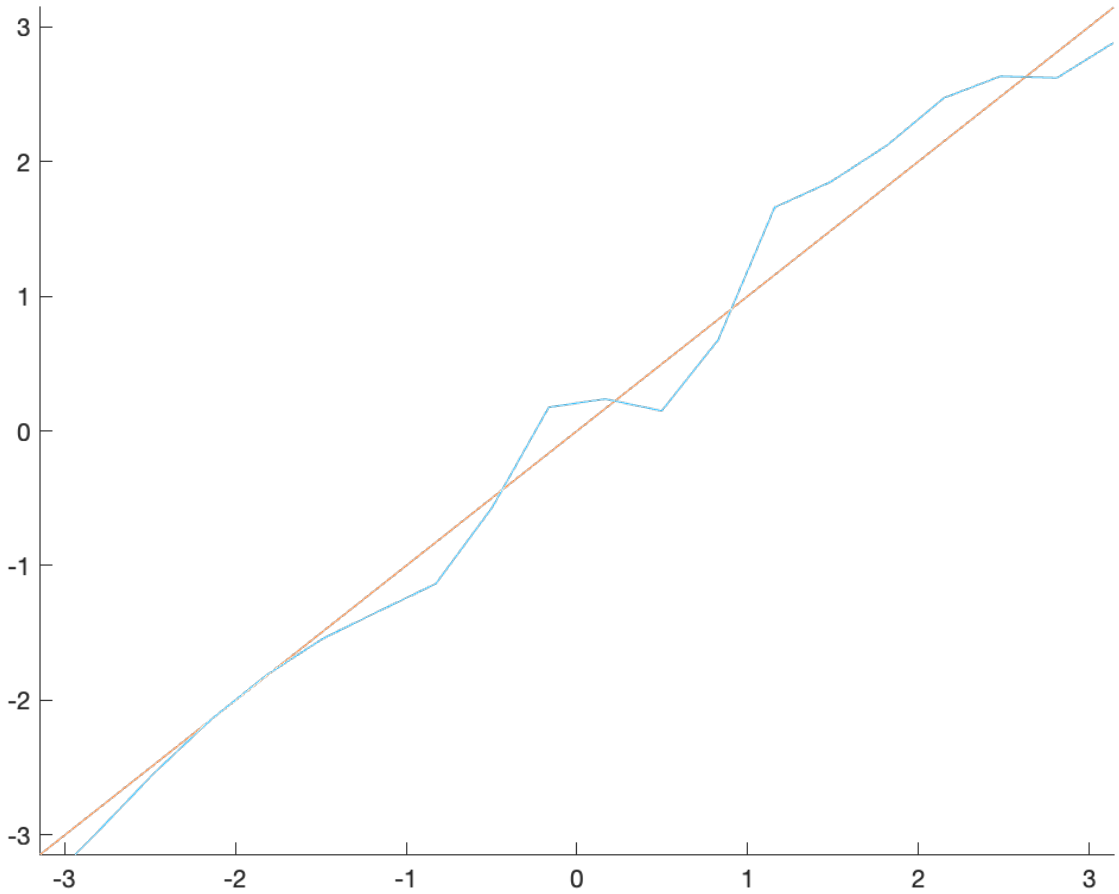


Figure 8: Multipath error (red: AoA estimate without multi-path, blue: AoA estimate with multi-path)

As it can be seen in figure 8, the error due to multi-path is significant. This error may degrade the performance of the experimental prototypes described in the next section.

4 Experimental results

Two prototypes have been developed to test the theory. The first one consists of an ultra-wide band device that transmits at 6GHz, a widely used device for ToA localisation. The second one makes use of a USRP software-defined radio that can emit at any frequency from 50MHz to 2.2GHz. The algorithms developed in section 2 have been tested on both devices.

All prototypes comply with the main functional block diagram, depicted in figure 9. The latter highlights what functions the given prototype must accomplish.

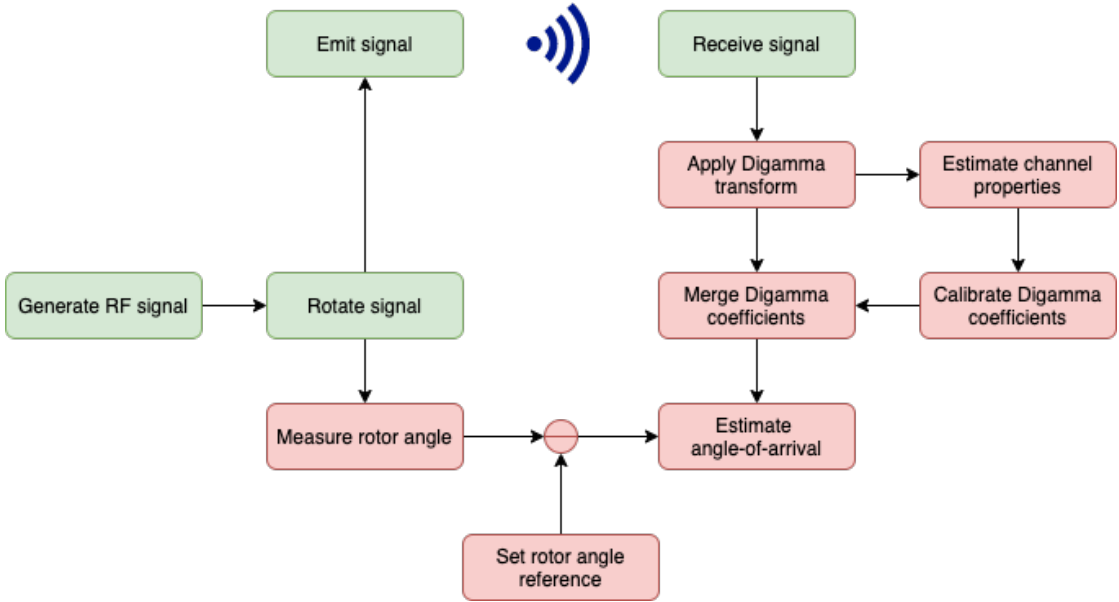


Figure 9: System functional block diagram

As presented in the previous sections, the idea is to generate an arbitrary RF signal and transmit it with a rotating antenna. On the receiver side, the signal is acquired and post-processed with the algorithms described in section 2. The unknowns of the environment will likely alter the received signal. This motivated the need to add a calibration function that will adjust the Digamma coefficients such as to eliminate the antenna phase variations.

In the following sections, for each prototype, the system architecture will be presented. It consists of the software, mechanical and electrical block diagrams, all derived from the main functional block diagram. Together, these four block diagrams can be considered as a complete representation of the system architecture.

Then, the system design, i.e. the implementation of the system architecture, will be presented and justified.

Finally, the experimental protocol and results will be presented and discussed.

4.1 UWB radio prototype

4.1.1 System architecture

The ultra-wide band device used for the first prototype is a DWM1001-DEV from Qorvo. Two such devices were used to build the system. One as a transmitter and the other one

as a receiver.

The mechanical system consists of a brushless DC motor from Maxon that drives directly a rotating structure. On the border of this rotating platform, a DWM1001-DEV device is fixed and counterweighted. A rechargeable Li-ion battery is used to power the device. Its centre-of-gravity is set at the center of rotation of the platform. The three phases of the Maxon motor are driven by a standalone motor controller. The control loop of this controller is closed by an encoder on the motor shaft and the encoder feedback is transmitted to the computer through an industry-standard RS-485 bus. Figure 10 illustrates this architecture.

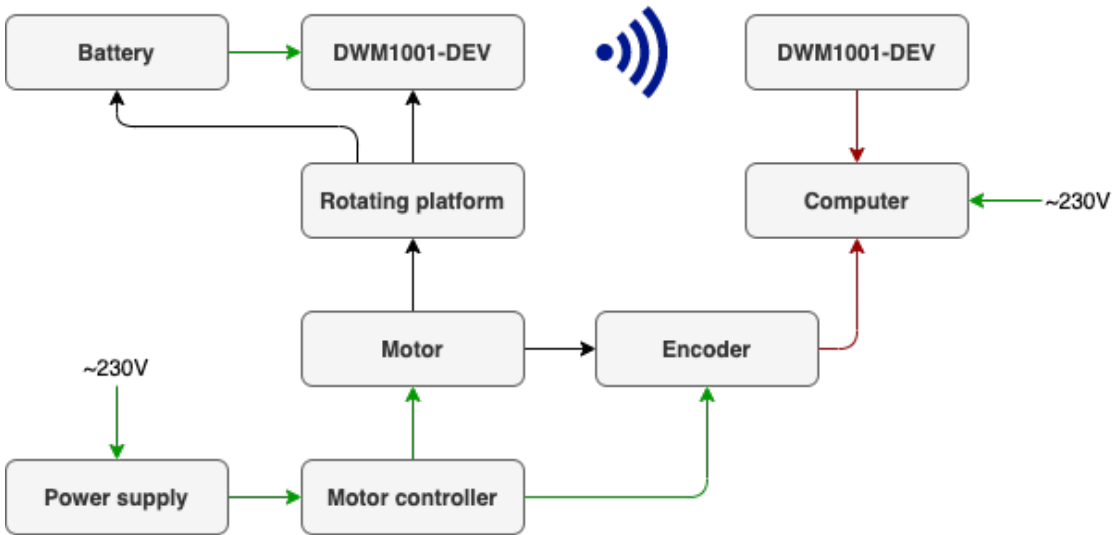


Figure 10: Mechanical architecture for the DWM prototype

The electrical system can therefore be divided into three subsystems: the transmission, acquisition and actuator subsystems.

The transmission subsystem consists of a Li-ion battery and a DWM1001-DEV device. Indeed, the purpose of this first subsystem is only to send a constant carrier signal. In this regard, it is completely independent from the other subsystems.

The acquisition subsystem consists of a DWM1001-DEV device and a computer. The two devices communicate through an USB bus and are used to estimate the relative angle between the two DWM1001-DEV devices.

The actuator subsystem drives the motor to induce a doppler effect on the rotating platform. A closed-loop control system allows a brushless DC motor to be controlled thanks to the feedback from an embedded encoder.

Note that there is a data interface between the actuator and the acquisition subsystem, which allows the encoder feedback to be transmitted to the acquisition system.

The block diagram in figure 11 depicts the different aspects of the electrical system architecture.

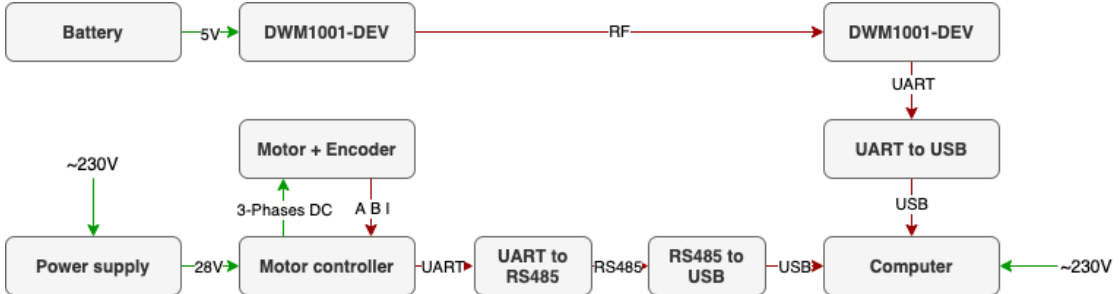


Figure 11: Electrical architecture for the DWM prototype

Finally, the software architecture was designed to be as modular as possible. The transmission and acquisition subsystem were designed to share the same codebase, based on Zephyr RTOS, along with a more implementation-specific code that will respectively handle the transmission and reception of data packets.

The codebase is decomposed into multiple functional units. The “runtime” unit manages the launch and management of the system tasks at the startup. On the one hand, the “IO” unit provides a high-level interface to the drivers and manages the transmission and reception of data packets within the acquisition subsystem. On the other hand, the “Drivers” unit provides a low-level interface between the communication busses and the “IO” unit. It mainly consists of code developed by the Decawave and ZephyrSDK developers. In addition, a “Debug” unit gives the capability of real-time debugging by providing a “Terminal” accessible by the user.

The motor controller in the actuator subsystem uses a firmware provided by STMicroelectronics [9] and was barely modified.

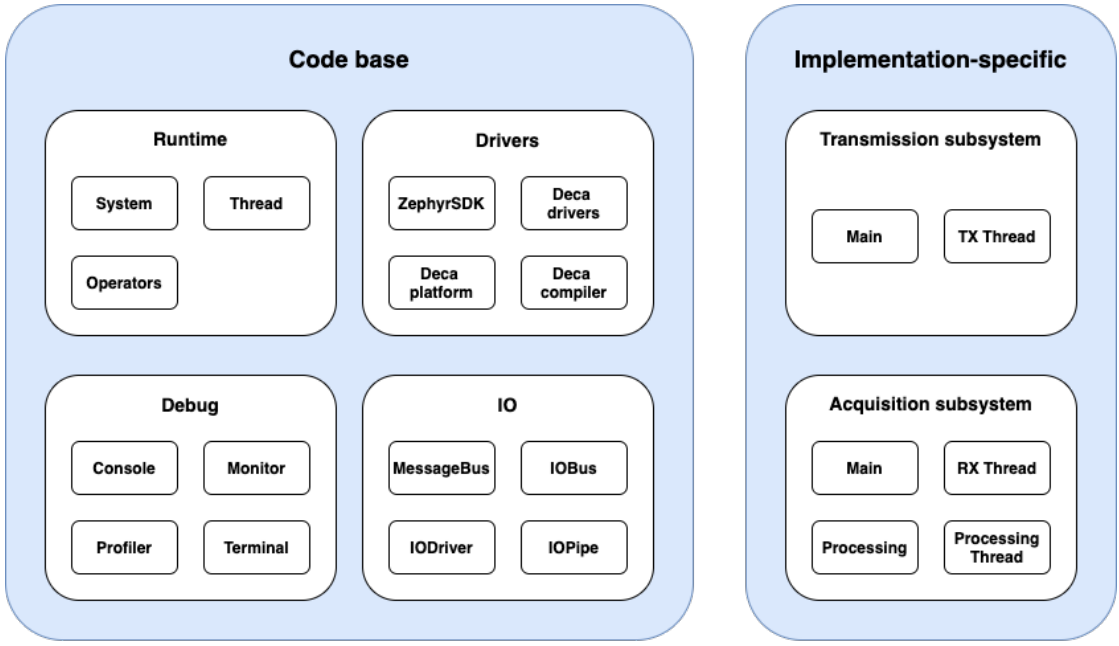


Figure 12: Software architecture for the DWM prototype

4.1.2 System design

This subsection describes into greater details how every part of the system was designed.

Hardware design The actuator subsystem is centred around the EC-i 40 motor from Maxon motors, along with its ENX 16 EASY highly accurate encoder. An ARM Cortex-M0 microcontroller allows a seamless closed-loop control of the motor after having tuned an internal **PID**. The control board hardware and firmware were developed by STMicroelectronics. Nevertheless, the firmware had to be slightly modified to send the encoder feedback to an RS-485 bus using the Modbus RTU protocol. This industry-standard protocol has the advantage of encoding a checksum for every sent data. This way, the acquisition subsystem can discard any corrupted data that would be inadvertently sent through the bus.

A standard lab power supply powers the motor controller at constant voltage of 28V.

Even though the EC-i 40 motor seems to be a standalone solution, its motor shaft had to be manually reworked to add a symmetrical 10mm flat on the edges of the shaft. This way, the motor could transmit the mechanical motion to the rotating platform.

The latter is designed as a 3D-printed “blade”, a mainly rectangular **PETG** extrusion. Mounting holes at the edge of this extrusion enable the placement of the DWM-1001DEV

device and a counterweight on the opposite side. Moreover, a cylindrical slot is installed in the middle of the blade to hold the battery. In addition to tolerance fitting, small enclosures allow the battery to be secured by zip-ties. Finally, the whole blade structure is secured to the motor shaft thanks to two airfoils on the sides of the structure. These airfoils give a negative lift to the whole structure and secure it to the motor shaft.

A commercial portable battery (5V, 3000mAh, max. 1A) is used to power the rotating DWM-1001DEV microcontroller.

In the acquisition subsystem, the receiver DWM1001-DEV device is simply connected to the computer with a Micro-USB cable.

The final assembly of the whole system is shown in figure 13.



Figure 13: Final assembly for DWM prototype

Software design For the sake of simplicity and modularity, the two DWM1001-DEV radios use the same C++ codebase. Indeed, a common framework was developed to manage the creation and management of tasks, the debugging and access to external peripherals. This framework is mainly based on the Avionics framework used by EPFL Xplore and the EPFL Rocket Team. In addition, a standalone library called RoCo (Rover Communication) was also used to communicate between the DWM1001-DEV and the acquisition system. This library pertains to provide a robust and lightweight communication protocol between a set of devices. It was deemed relevant to use in the context of this project.

On the one hand, the software of the transmission subsystem consists of a single “TXThread” task that continuously sends packets with constant data values in it.

On the other hand, the acquisition system is divided into multiple tasks that run concurrently. The RXThread acquires the transmitted packets and estimates the phase delay between emitter and receiver. A method made available in the Decawave firmware allows the extraction of the **CFO**. The proprietary `dwt_readcarrierintegrator` function returns the phase drift between the emitter and the receiver. This value is exactly what is needed to apply the digamma transform and recover the **AoA**.

Subsequently, the received phase drift estimate is passed to a buffering stage in the “Processing” class and retrieved by the “ProcessingThread” task. The latter task finally sends the phase drift estimate via the RoCo protocol through a Serial interface. The buffering stage standing between “RXThread” and the “ProcessingThread” allows a pipelined execution of the threads.

After that the data is acquired on the computer, a Matlab code could be run to apply the digamma transform and whether or not the **AoA** could be successfully retrieved.

As already mentioned, the firmware of the motor controller was barely modified, so that it could transmit the encoder’s absolute position to the acquisition system.

4.1.3 Experimentation

Multiple experiments were performed with this experimental setup. The rotation speed of the actuator subsystem was gradually adjusted from 100rpm to 1200rpm and the phase drift estimate was recorded on the computer.

In every case, a significant phase drift was observed, yet unfortunately, it was unrelated to the theoretical predictions. It is now believed that the significant accelerations encountered during the rotation of the device may have affected the crystal oscillator on the device, thereby causing significant clock errors and making the real doppler effect undetectable.

Moreover, since the DWM1001-DEV is a proprietary device, it is highly difficult to isolate hardware issues and understand how the `dwt_readcarrierintegrator` function estimates the phase drift.

From a system point-of-view, it appeared that using a better documented and more flexible device would minimise the project failure risk and eventually give better results, even though this decision discarded the working hours spent on the first prototype.

4.2 USRP radio prototype

4.2.1 System architecture

This second prototype makes use of a NI-USRP-2920 software-defined radio. This device can transmit at any frequency in the range from 50MHz to 2.2GHz. The advantage of this devices over the DWM1001-DEV comes from its flexibility in sending any signal at any frequency. In addition, the USRP was configured to work with GNU radio, a well documented framework for transmitting and receiving RF signals. This radio is also capable of handling the reception and transmission of data simultaneously and on the same device. The only drawback of this radio is its weight of 1.2kg.

The new software framework and the heavy weight of the USRP enforced a complete mechanical and software redesign of system. Nevertheless, the same motor and motor controllers could be reused, thereby only implying a partial redesign of the electrical system.

As mentioned, the mechanical system had to be rethought. In particular, it was not possible to include the USRP device on a rotating platform as it was too heavy. Instead, the USRP is now fixed on the stator side of the actuator and only the antenna is left on the rotor side. The interface between the static USRP and the rotating antenna is now a dedicated RF slip ring that can transmit RF signals between a stator and a rotor. It then becomes obvious that a direct drive of the antenna is not possible anymore because the center of rotation of the platform is already occupied by the RF slip ring. This motivated the need for a gearing system between the motor driving shaft and the slip ring. The updated mechanical block diagrams is now depicted in figure 14.

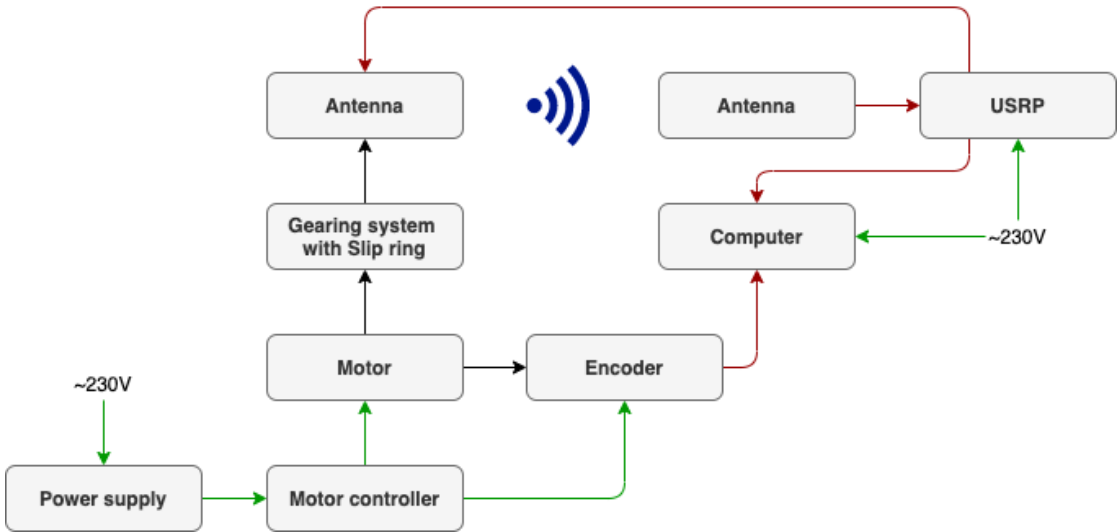


Figure 14: Mechanical architecture for the USRP prototype

The electrical system is similar to the one developed for the first prototype. Indeed, the only difference is that there is a single USRP device instead of two DWM1001 devices. Moreover, the USRP is now interfaced through an Ethernet bus with the computer. Figure 15 presents the updated electrical architecture.

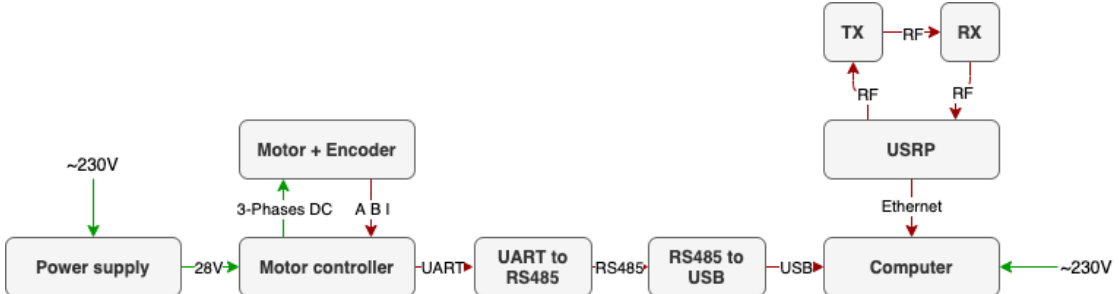


Figure 15: Electrical architecture for the USRP prototype

Finally, the software architecture had to be completely rethought. The USRP is now solely based on the GNU radio firmware and cannot be considered as an embedded device anymore. The framework developed for the first prototype could therefore not be used for the USRP.

The software is now developed in Python and a single program handles the transmission, reception and processing of the received data. Since the GNU radio framework is very high-level, only the post-processing steps had to be developed. In this regard, each step is considered as a single Python class and the hierarchy of these steps are depicted

in the block diagram in figure 16. These steps will be further described in the next section.

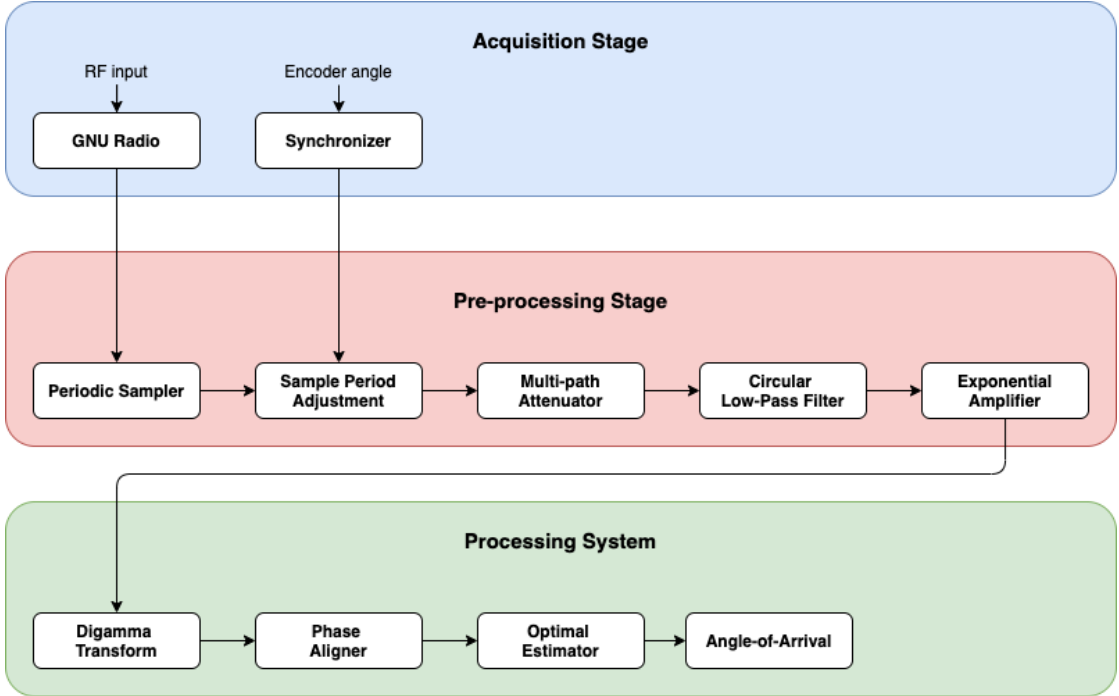


Figure 16: Software architecture for the USRP prototype

4.2.2 System design

Hardware design The motor used for the second prototype is again a EC-40i brushless DC motor from Maxon and it is controlled with the same hardware. Since the mechanical system for this prototype is slightly more complicated than with the first prototype, a custom casing was built to better secure the gearing system. The casing consists of two laser-cut plywood panels, on which the RF slip ring and the Maxon motor are attached. The plywood panels are mounted together using Aluminum extrusions. In addition, two 3D-printed gears enforce the transmission of the mechanical motion of the motor shaft to the slip ring. Since the slip ring was found to be subject to a lot of friction, it was decided to use a reduction factor of 1:10 on the gearing system, such that less stress is incurred to the motor. The figure 17 illustrates the final mechanical assembly. The other mechanical or electrical design considerations are derived from the first prototype.

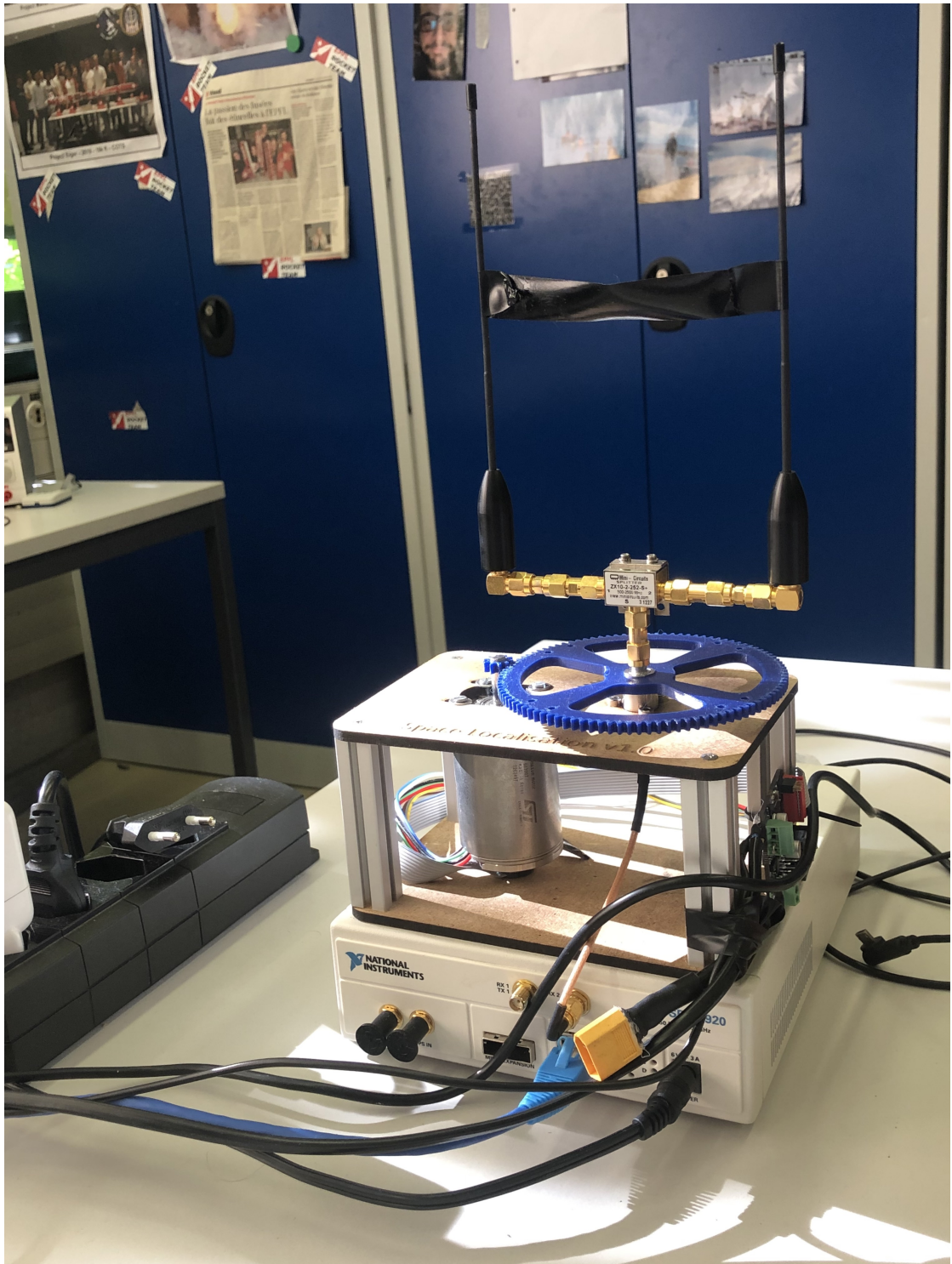


Figure 17: USRP prototype final assembly

Software design The GNU radio framework was employed to develop the whole second prototype's software. Since this framework is very high-level, there was no need to make a higher-level abstraction, as with the first prototype. Instead, the focus could be exclusively set on the data extraction stage. As in figure 16, the estimation of the **AoA** can be divided into three main stages: the acquisition, pre-processing and estimation stages.

The acquisition stage interfaces the GNU radio framework with the algorithms that were developed for this project. It allows the transmitter and receiver channels to be configured and transfers the received data to the pre-processing stage. This stage also fetches the encoder data from the RS485 bus and passes it to the algorithmic steps that need it.

The pre-processing stage pertains to treat the incoming data and address timing, distortion and noise issues. It also prepares the final signal before applying the Digamma transform.

The estimation stage applies the Digamma transform to the pre-processed signal. The multi-path effects are then attenuated from the signal and the phase is realigned to account for other environmental unknowns. Finally, an optimal estimator allows the **AoA** to be estimated.

Finally, the **AoA** is plotted in real-time on the computer.

The pre-processing stage and estimation stages can be further divided into algorithmic units. Each of these is implemented as separate Python classes to increase the modularity of the whole system. These building blocks are listed hereunder:

Periodic Sampler Acquires data samples from the RF input stream. Every time the antenna makes a full rotation, the sampler is reset, such that the data samples are processed period by period.

Sample Period Adjuster The motor controller might not exactly reproduce the desired rotating frequency. In this regard, the measured period must be synchronised with the motor's motion and this action is performed by the Sample Period Adjuster thanks to the received encoder input.

Gain&Phase Corrector DC bias, constant phase errors might affect the measurements. The Gain&Phase Corrector's purpose is to cancel out the mean phase offset and

compensate the signal DC bias by dividing it by its maximum.

Circular Filter The USRP demodulation seemed to add noise components at around 20Hz. A low-pass filter had to be applied to remove this undesired noise. Nonetheless, standard filtering methods could not be directly used since they added “border effects” at both ends of the signal, a well-known artefact of convolutional filters. These distortions affected the quality of the **AoA** estimation. To prevent this issue, the standard filtering function had to be reimplemented, so that the fact that the signal is periodic was used to remove the filtering “border effects”.

Exponential Amplifier As per equation (30), the signal had to be exponentially amplified before applying the Digamma transform theory.

Digamma Transform The implementation of this building block derives directly from the definition of the Digamma transform in equation (32).

Phase Aligner The Digamma coefficients may be distorted by the antenna phase variations and the environment. With a beforehand calibration, the phase aligner can attenuate these undesirable effects, as discussed in section 2.4.

Optimal Estimator Finally, the Digamma coefficients can be merged, so that the estimator achieving the Cramer-Rao lower bound is obtained. The **AoA** is now ready to be used.

4.2.3 Experimentation

The system described in the previous section was extensively tested in different environments and with two different carrier frequencies: 400MHz and 1.2GHz. The transmitter antenna was set at a rotation frequency of 2Hz, after the gear reduction.

A custom testbench was designed to move the receiver antenna at extremely precise locations. Indeed, a laser-cutter 2D CNC was assembled and the receiver antenna was mounted instead of the laser. The final assembly of this device is shown in figure 18.

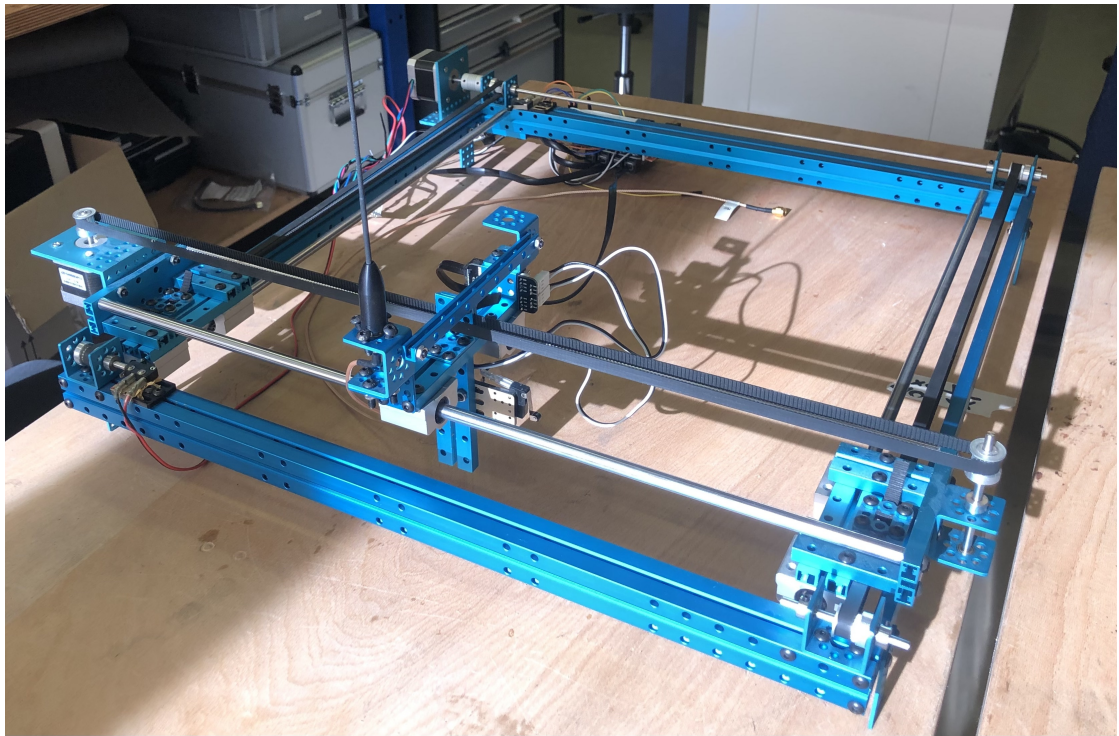


Figure 18: Customized CNC laser-cutter for the experimental setup

To control this CNC, an Arduino was programmed with the so-called GRBL firmware. This firmware allows an external computer to send directional instructions (e.g. move right 10mm, move down 1mm, ...) to the CNC. A file containing a set of these instructions (G-code) was written to replace the need of an experimental protocol and could be sent with the Universal Gcode Platform open-source software [10]. The “Experiment.gcode” file contains instructions to move the antenna by 10mm every 30 seconds.

The experimental protocol could be simplified to the following:

- 1) Setup the Ethernet connection with the USRP
- 2) Launch the SpaceLocalisation software with “python3.9 Main.py”
- 3) Launch the Universal Gcode Platform
- 4) Load the Gcode file “Experiment.gcode”
- 5) Execute the Gcode file “Experiment.gcode” on the CNC
- 6) The experiment is now autonomously conducted
- 7) When the Gcode instructions are completed, the evolution of the angle-of-arrival is plotted on the computer and logged as a data file.

This experimental protocol was run and the results collected. Figure 19 depicts the resulting angle estimations.

Between the different measurements, a standard error of 0.2° was observed. The orange curve shows the theoretical observations and the blue curve illustrates the angle estimation after measurements. Overall, the blue curve and the orange curve coincide. It is believed that the remaining bias between the two curves is due to multi-path effects and must be investigated separately. Interestingly, an overshoot of the angle estimator occurs when the receiving antenna starts moving. This phenomenon is likely due to the deflection of the flexible antenna, which oscillates a little at the beginning of every motion. Nevertheless, it is an undesired effect that must also be studied, especially since it could greatly affect moving receivers, such as rovers.

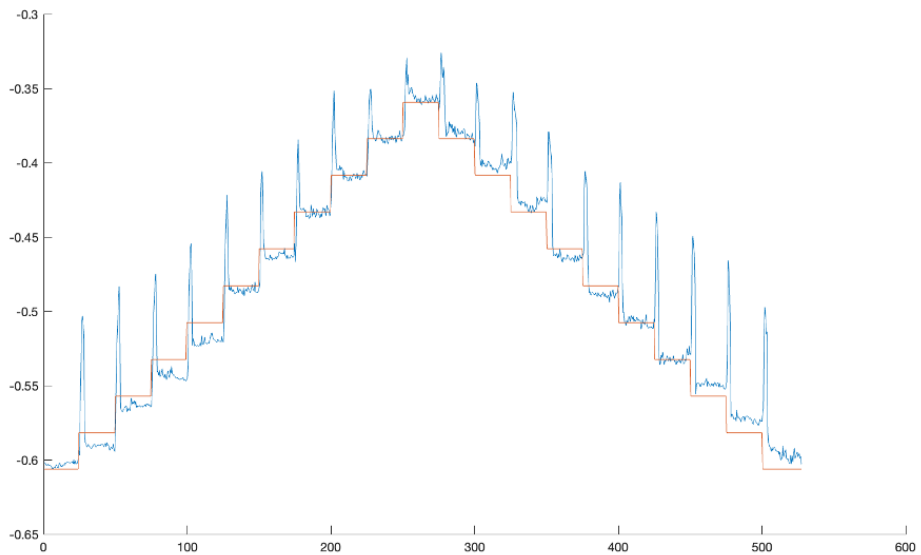


Figure 19: Experimental results following the aforementioned protocol

Figure 20 is a detailed view of Figure 19. It attempts to illustrate the low variance of the Digamma estimator. As mentioned before, the standard error goes down to 0.2° at a 1m distance and oscillates when the receiver is moving from one angle to another one.

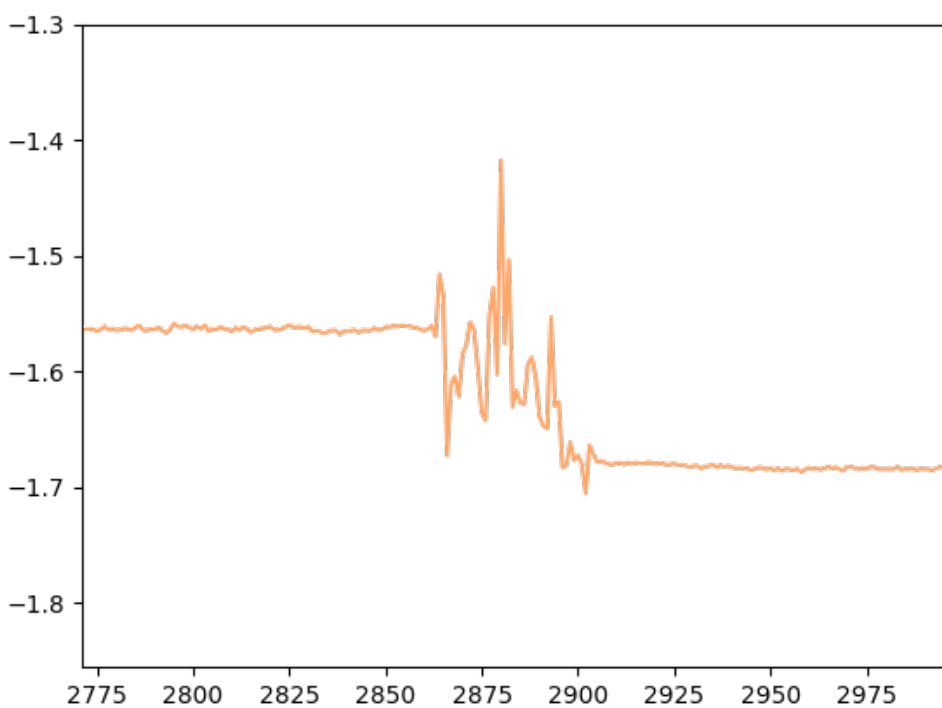


Figure 20: Detailed view of the experimental results

5 Future work

This semester project is the first building block of a robust localisation method, especially intended for areas without GNSS coverage. Further research might be performed to generalise this localisation method to three dimensions. The theory should be easily generalisable. However, building a system with an antenna rotating along two axes will not be an easy task.

An additional assessment of the environmental effects that affect the transmission channel could also be performed to complete the channel model described in equation (8).

The theoretical framework could also be completed by including more validations of the approximations that were performed, especially in section 2.4.

Finally, the design of a custom antenna, rigid, and completely aligned with the rotation axis could help reducing the errors in **AoA** estimation for the USRP prototype. This could attenuate the overshooting effects that appeared during the experiments. Moreover, a hardware method [11] to attenuate multi-path effects makes use of polarised antennas. Using this method could help cancelling-out the secondary path that are only reflected once and that may affect the quality of the experiment.

6 Conclusion

The initial motivation of this project was to research promising localisation methods, especially for space applications. I believed that the **AoA** was an underestimated, yet promising localisation method.

In fact, the main critic on this method [7] was that it was highly sensitive to multi-path effects, especially in urban areas. The latter argument might not be as strong for lunar environment for instance. Furthermore, it was shown that the Digamma estimator could achieve the Cramer-Rao lower bound and remove the antenna phase variations.

The main contribution of this semester project is without any doubt the theoretical framework involving the Digamma transform and its interesting properties. In addition to developing and proving most of the statements concerning this mathematical tool, the framework was also thoroughly validated thanks to Matlab simulation and finite-element analyses.

Furthermore, the development of two prototypes to test the theory in real-life has shown the potential of this method. Indeed, a localisation accuracy of 0.2° at 1m distance could be achieved, even by only using non-specialised hardware. Using state-of-the-art and specialised hardware could dramatically enhance the system's performance.

Officially, the scope of the project was only to research **AoA** localisation methods and simulate them. Yet, two prototypes were designed and experimental results could be extracted.

Remark that this project acts a starting point for further research: many aspects mentioned in section 6 were not covered by this semester project and may be further researched.

I would like to thank Prof. Andreas Burg, Associate Professor of the EPFL Telecommunications Circuits Laboratory, David Rodríguez, PhD at EPFL Space Center, and particularly Sitian Li, Doctoral Assistant at the Telecommunications Circuits Laboratory, who spent countless hours advising me and helping me overcoming difficult theoretical steps.

List of Abbreviations

AoA Angle-of-Arrival: Method to estimate the relative angle between an emitter and a receiver. [1](#), [2](#), [3](#), [6](#), [7](#), [9](#), [11](#), [13](#), [14](#), [15](#), [16](#), [17](#), [18](#), [19](#), [21](#), [28](#), [33](#), [34](#), [38](#), [39](#)

AWGN Additive White Gaussian Noise: Standard noise model in telecommunication channels. [3](#), [8](#), [9](#), [11](#), [18](#)

CFO Carrier frequency offset: the extent to which the received signal carrier deviates from the local clock. [5](#), [28](#)

PETG Polyethylene terephthalate glycol: Common plastic material, often used in 3D-printing. [25](#)

PID Proportional-Integral-Derivative: Widely used control loop architecture, widely used for actuators. [25](#)

PLL Phase-Locked Loop: Control loop that locks to a specific frequency component. [4](#), [5](#)

TDoA Time-Difference-of-Arrival: Similar to Time-of-Arrival but uses the time a signal needs to travel and come back to an emitter. [3](#)

ToA Time-of-Arrival: Method to estimate the relative distance between an emitter and a receiver. [3](#), [21](#)

References

- [1] *Selective availability*. [Online]. Available: <https://www.gps.gov/systems/gps/modernization/sa/>.
- [2] A. Delépaut, P. Giordano, J. Ventura-Traveset, D. Blonski, M. Schönfeldt, P. Schoonejans, S. Aziz, and R. Walker, "Use of gnss for lunar missions and plans for lunar in-orbit development," *Advances in Space Research*, vol. 66, May 2020. DOI: [10.1016/j.asr.2020.05.018](https://doi.org/10.1016/j.asr.2020.05.018).
- [3] B. Khaleghi, A. Khamis, F. O. Karray, and S. N. Razavi, "Multisensor data fusion: A review of the state-of-the-art," *Information Fusion*, vol. 14, no. 1, pp. 28–44, 2013, ISSN: 1566-2535. DOI: <https://doi.org/10.1016/j.inffus.2011.08.001>. [Online]. Available: <https://www.sciencedirect.com/science/article/pii/S1566253511000558>.
- [4] L. V. Ksanfomality, "Luna-5 (1965): Some results of a failed mission to the moon," *Cosmic Research*, vol. 56, no. 4, pp. 276–282, 2018. DOI: [10.1134/S0010952518040020](https://doi.org/10.1134/S0010952518040020). [Online]. Available: <https://doi.org/10.1134/S0010952518040020>.
- [5] H. A. Obeidat, I. Ahmad, M. R. Rawashdeh, A. A. Abdullah, W. S. Shuaieb, O. A. Obeidat, and R. A. Abdallhameed, "Enhanced toa estimation using ofdm over wide-band transmission based on a simulated model," *Wireless Personal Communications*, vol. 123, no. 4, pp. 3449–3461, 2022. DOI: [10.1007/s11277-021-09297-z](https://doi.org/10.1007/s11277-021-09297-z). [Online]. Available: <https://doi.org/10.1007/s11277-021-09297-z>.
- [6] I. Jami and R. Ormondroyd, "Improved method for estimating angle of arrival in multipath conditions using the 'music' algorithm," in *2000 IEEE-APS Conference on Antennas and Propagation for Wireless Communications (Cat. No.00EX380)*, 2000, pp. 99–102. DOI: [10.1109/APWC.2000.900151](https://doi.org/10.1109/APWC.2000.900151).
- [7] E. Al-Ardi, R. Shubair, and M. Al-Mualla, "Direction of arrival estimation in a multipath environment: An overview and a new contribution," *Applied Computational Electromagnetics Society Journal*, vol. 21, pp. 226–238, Nov. 2006.
- [8] D. Belega, D. Petri, and D. Dallet, "Amplitude and phase estimation of real-valued sine wave via frequency-domain linear least-squares algorithms," *IEEE Transactions on Instrumentation and Measurement*, vol. 67, no. 5, pp. 1065–1077, 2018. DOI: [10.1109/TIM.2017.2785098](https://doi.org/10.1109/TIM.2017.2785098).
- [9] *Compact reference design kit for robotics and automation based on stspin32f0a*. [Online]. Available: <https://www.st.com/en/evaluation-tools/evalkit-robot-1.html>.
- [10] *Universal gcode sender: A full featured gcode platform used for interfacing with advanced cnc controllers*. [Online]. Available: <https://winder.github.io/ugs-website/>.
- [11] L. Xie, X. Cui, S. Zhao, and M. Lu, "Mitigating multipath bias using a dual-polarization antenna: Theoretical performance, algorithm design, and simulation," *Sensors*, vol. 17, p. 359, Feb. 2017. DOI: [10.3390/s17020359](https://doi.org/10.3390/s17020359).